

Parity-violating electroweak asymmetry in $\bar{e}p$ scattering

K. A. Aniol¹, D. S. Armstrong³⁴, T. Averett³⁴, M. Baylac^{27,12}, E. Burtin²⁷,
 J. Calarco²⁰, G. D. Cates^{24,33}, C. Cavata²⁷, Z. Chai¹⁹, C. C. Chang¹⁷, J.-P. Chen¹²,
 E. Chudakov¹², E. Cisbani¹¹, M. Coman⁴, D. Dale¹⁴, A. Deur^{12,33}, P. Djawotho³⁴,
 M. B. Epstein¹, S. Escoffier²⁷, L. Ewell¹⁷, N. Falletto²⁷, J. M. Finn^{34,*}, K. Fissum¹⁹,
 A. Fleck²⁵, B. Frois²⁷, S. Frullani¹¹, J. Gao^{19,†}, F. Garibaldi¹¹, A. Gasparian⁷,
 G. M. Gerstner³⁴, R. Gilman^{26,12}, A. Glamazdin¹⁵, J. Gomez¹², V. Gorbenko¹⁵,
 O. Hansen¹², F. Hersman²⁰, D. W. Higinbotham³³, R. Holmes²⁹, M. Holtrop²⁰,
 T.B. Humensky^{24,33,‡}, S. Incerti³⁰, M. Iodice¹⁰, C. W. de Jager¹², J. Jardillier²⁷, X. Jiang²⁶,
 M. K. Jones^{34,12}, J. Jorda²⁷, C. Jutier²³, W. Kahl²⁹, J. J. Kelly¹⁷, D. H. Kim¹⁶,
 M.-J. Kim¹⁶, M. S. Kim¹⁶, I. Kominis²⁴, E. Kooijman¹³, K. Kramer³⁴, K. S. Kumar²⁴
 .¹⁸, M. Kuss¹², J. LeRose¹², R. De Leo⁹, M. Leuschner²⁰, D. Lhuillier²⁷, M. Liang¹²,
 N. Liyanage^{19,12,33}, R. Lourie²⁸, R. Madey¹³, S. Malov²⁶, D. J. Margaziotis¹, F. Marie²⁷,
 P. Markowitz¹², J. Martino²⁷, P. Mastromarino²⁴, K. McCormick²³, J. McIntyre²⁶,
 Z.-E. Meziani³⁰, R. Michaels¹², B. Milbrath³, G. W. Miller²⁴, J. Mitchell¹², L. Morand⁵
 .²⁷, D. Neyret²⁷, C. Pedrisat³⁴, G. G. Petratos¹³, R. Pomatsalyuk¹⁵, J. S. Price¹²,
 D. Prout¹³, V. Punjabi²², T. Pussieux²⁷, G. Quéméner³⁴, R. D. Ransome²⁶,
 D. Relyea²⁴, Y. Roblin², J. Roche³⁴, G. A. Rutledge^{34,32}, P. M. Rutt¹², M. Rvachev¹⁹,
 F. Sabatie²³, A. Saha¹², P. A. Souder^{29,§}, M. Spradlin^{24,8}, S. Strauch²⁶, R. Suleiman¹³
 .¹⁹, J. Templon⁶, T. Teresawa³¹, J. Thompson³⁴, R. Tieulent¹⁷, L. Todor²³,
 B. T. Tonguc²⁹, P. E. Ulmer²³, G. M. Urciuoli¹¹, B. Vlahovic²¹, K. Wijesooriya³⁴,
 R. Wilson⁸, B. Wojtsekhowski¹², R. Woo³², W. Xu¹⁹, I. Younus²⁹, and C. Zhang¹⁷

(The HAPPEX Collaboration)

¹ *California State University - Los Angeles,*

Los Angeles, California 90032, USA

² *Université Blaise Pascal/IN2P3, F-63177 Aubièrre, France*

³ *Eastern Kentucky University, Richmond, Kentucky 40475, USA*

⁴ *Florida International University, Miami, Florida 33199, USA*

⁵ *Université Joseph Fourier, F-38041 Grenoble, France*

⁶ *University of Georgia, Athens, Georgia 30602, USA*

- ⁷ *Hampton University, Hampton, Virginia 23668, USA*
- ⁸ *Harvard University, Cambridge, Massachusetts 02138, USA*
- ⁹ *INFN, Sezione di Bari and University of Bari, I-70126 Bari, Italy*
- ¹⁰ *INFN, Sezione di Roma III, 00146 Roma, Italy*
- ¹¹ *INFN, Sezione Sanità, 00161 Roma, Italy*
- ¹² *Thomas Jefferson National Accelerator Laboratory,
Newport News, Virginia 23606, USA*
- ¹³ *Kent State University, Kent, Ohio 44242, USA*
- ¹⁴ *University of Kentucky, Lexington, Kentucky 40506, USA*
- ¹⁵ *Kharkov Institute of Physics and Technology, Kharkov 310108, Ukraine*
- ¹⁶ *Kyungpook National University, Taegu 702-701, Korea*
- ¹⁷ *University of Maryland, College Park, Maryland 20742, USA*
- ¹⁸ *University of Massachusetts Amherst,
Amherst, Massachusetts 01003, USA*
- ¹⁹ *Massachusetts Institute of Technology,
Cambridge, Massachusetts 02139, USA*
- ²⁰ *University of New Hampshire, Durham, New Hampshire 03824, USA*
- ²² *Norfolk State University, Norfolk, Virginia 23504, USA*
- ²¹ *North Carolina Central University,
Durham, North Carolina 27707, USA*
- ²³ *Old Dominion University, Norfolk, Virginia 23508, USA*
- ²⁴ *Princeton University, Princeton, New Jersey 08544, USA*
- ²⁵ *University of Regina, Regina, Saskatchewan S4S 0A2, Canada*
- ²⁶ *Rutgers, The State University of New Jersey,
Piscataway, New Jersey 08855, USA*
- ²⁷ *CEA Saclay, DAPNIA/SPhN, F-91191 Gif-sur-Yvette, France*
- ²⁸ *State University of New York at Stony Brook,
Stony Brook, New York 11794, USA*
- ²⁹ *Syracuse University, Syracuse, New York 13244, USA*
- ³⁰ *Temple University, Philadelphia, Pennsylvania 19122, USA*

³¹ *Tohoku University, Sendai 9890, Japan*

³² *TRIUMF, Vancouver, British Columbia V6T 2A3, Canada*

³³ *University of Virginia, Charlottesville, Virginia 22901, USA and*

³⁴ *College of William and Mary, Williamsburg, Virginia 23187, USA*

(Dated: May 7, 2019)

Abstract

We have measured the parity-violating electroweak asymmetry in the elastic scattering of polarized electrons from protons. Significant contributions to this asymmetry could arise from the contributions of strange form factors in the nucleon. The measured asymmetry is $A = -15.05 \pm 0.98(\text{stat}) \pm 0.56(\text{syst})$ ppm at the kinematic point $\langle\theta_{\text{lab}}\rangle = 12.3^\circ$ and $\langle Q^2 \rangle = 0.477$ (GeV/c)². Based on these data as well as data on electromagnetic form factors, we extract the linear combination of strange form factors $G_E^s + 0.392G_M^s = 0.014 \pm 0.020 \pm 0.010$ where the first error arises from this experiment and the second arises from the electromagnetic form factor data. This paper provides a full description of the special experimental techniques employed for precisely measuring the small asymmetry, including the first use of a strained GaAs crystal and a laser-Compton polarimeter in a fixed target parity-violation experiment.

PACS numbers: 13.60.Fz; 11.30.Er; 13.40.Gp; 14.20.Dh

*Electronic address: finn@physics.wm.edu

†Now at: Duke University, Durham, North Carolina 27708 USA

‡Now at: University of Chicago, IL, 60637, USA

§Electronic address: souder@phy.syr.edu

I. INTRODUCTION

In recent years, the role of strange quarks in nucleon structure has been a topic of great interest. Data from the European Muon Collaboration (EMC) [1] showed that valence quarks contribute less than half of the proton spin and also suggested that significant spin may be carried by the strange quarks. Based on these observations, Kaplan and Manohar [2] pointed out that strange quarks might also contribute to the magnetic moment and charge radius of the proton, *i.e.* to the vector matrix elements. It turns out that a practical way to measure these strange vector matrix elements is by measuring the electroweak asymmetry in polarized electron scattering [3, 4, 5].

In the work presented here, we have measured the parity-violating asymmetry $A = (\sigma_R - \sigma_L)/(\sigma_R + \sigma_L)$ where $\sigma_{R(L)}$ is the differential cross section for elastic scattering of right(*R*) and left(*L*) handed longitudinally polarized electrons from protons. The kinematics $\langle\theta_{\text{lab}}\rangle = 12.3^\circ$ and $\langle Q^2 \rangle = 0.477 \text{ (GeV/c)}^2$ correspond to the smallest angle and largest energy possible with the available spectrometers. Under reasonable assumptions for the Q^2 dependence of the strange form factors, these kinematics maximize the figure of merit for a first measurement. Results were obtained in two separate data-taking runs, in 1998 and 1999 in Hall A at the Thomas Jefferson National Accelerator Facility (Jefferson Lab). The experimental conditions were somewhat different in the two runs, here referred to as the “1998 run” and “1999 run”. In the 1998 run we used a 100 μA beam with 38% polarization produced from a bulk GaAs crystal. In the 1999 run we ran with a strained GaAs crystal with polarization $P=70\%$ and $I=35 \mu\text{A}$. This gave an improvement in P^2I , providing a greater effective rate of taking data, but also creating new challenges in controlling systematic errors. The 1999 run was subdivided into two periods of several weeks each, the primary difference being the availability of the Compton polarimeter, which provided an independent measurement of the beam polarization, for the latter part.

Brief reports of these results have been published [6, 7]; the present paper presents the experimental technique, data analysis, and physics implications in much more detail. Further details can be found in several dissertations [8, 9, 10, 11, 12, 13].

This paper is organized as follows. In section II we explain the motivation for this experiment. Section III covers the experimental method used to measure such small asymmetries of order 10 parts-per-million (ppm) in electron scattering. A crucial aspect of the measure-

ment is the control of systematic errors, as described in section IV. Section V discusses the data analysis of the asymmetries, the sensitivities to beam parameters, and the resulting helicity correlated systematic corrections due to the beam. In section VI the extracted physics asymmetry is presented with all corrections to the data including the beam polarization, backgrounds, Q^2 measurements, radiative corrections, kinematics, and acceptance. Section VII presents the results and their interpretation, which requires corrections for form factors. Section VII B provides the physics interpretation in the context of models of nucleon strangeness. Finally, VIII draws the conclusions of this work.

II. MOTIVATION

Measurements of the contribution of strange quarks to nucleon structure provide a unique window on the quark-antiquark sea and make an important impact on our understanding of the low-energy QCD structure of nucleons. Since the mass of the strange quark is comparable to the strong interaction scale it is reasonable to expect that strangeness $q\bar{q}$ pairs should make observable contributions to the properties of nucleons, for instance the mass, spin, momentum, and the electromagnetic form factors. Indeed, charm production in deep inelastic neutrino scattering [14] has shown that strange quarks carry about 3% of the momentum of the proton at $Q^2 = 2 \text{ (GeV/c)}^2$. Much of the interest in the strangeness content of the nucleon originates from the EMC experiment [1] and related recent experiments [15, 16] which studied the spin structure functions of the proton and neutron in deep inelastic scattering. These experiments have established that the Ellis-Jaffe sum rule [17] is violated and that relatively little of the proton's spin is carried by the valence quarks. The initial paper also suggested that significant spin was carried by strange quarks. More recent work has indicated that this latter conclusion is difficult to establish convincingly [18]; see also the recent reviews by Kumar and Souder [19], Beck and McKeown [20], Beck and Holstein [21], and Musolf *et al.* [22].

In the aftermath of the EMC results, it was suggested [2] that strange quarks might contribute to the vector matrix elements of the nucleon. Indeed, numerous calculations of strange matrix elements have been computed in the context of various models. The theoretical approaches include dispersion relations [23, 24, 25, 26], vector dominance models with $\omega - \phi$ mixing [27], the chiral bag model [28], unquenched quark model [29], perturbative

chiral quark model [30], light-cone diquark model [31], chiral quark model [32, 33], Skyrme model [34, 35], Nambu-Jona-Lasinio soliton model [36], meson-exchange models [37], kaon loops [38, 39, 40], an SU(3) chiral quark-soliton model [41], heavy baryon chiral perturbation theory [42, 43], quenched chiral perturbation theory [45], as well as lattice QCD calculations [44, 45]. These calculations have elucidated the physics behind strange matrix elements and have provided numerical estimates of the size of possible effects that have served for the design goals of our experiment.

Parity violating electron scattering is a practical method to measure the strange vector matrix elements [3, 4, 5]. Purely electromagnetic scattering at a given kinematics can measure only two linear combinations of the Sachs form factors:

$$G_{E,M}^{\gamma p} = \frac{2}{3}G_{E,M}^u - \frac{1}{3}G_{E,M}^d - \frac{1}{3}G_{E,M}^s \quad (1)$$

$$G_{E,M}^{\gamma n} = \frac{2}{3}G_{E,M}^d - \frac{1}{3}G_{E,M}^u - \frac{1}{3}G_{E,M}^s \quad (2)$$

where $G_{E,M}^f$ is the electric (E) or magnetic (M) form factor for quark flavor f in the proton. Here it is assumed that the quark flavors u , d , and s contribute. Charge symmetry between proton p and neutron n is also assumed, so that for the quark form factors

$$G_p^u = G_n^d ; \quad G_p^d = G_n^u ; \quad G_p^s = G_n^s \quad (3)$$

where now the subscripts p and n are for proton and neutron.

Additional information is needed to determine whether or not there is a contribution from the strangeness form factors $G_{E,M}^s$. This is provided by parity violation in the scattering from protons, measuring a new pair of linear combinations

$$G_{E,M}^{Zp} = \left(\frac{1}{4} - \frac{2}{3} \sin^2 \theta_W \right) G_{E,M}^u + \left(-\frac{1}{4} + \frac{1}{3} \sin^2 \theta_W \right) \times [G_{E,M}^d + G_{E,M}^s] \quad (4)$$

where Z stands for the Z^0 boson of the neutral weak interaction.

Thus by measuring these neutral weak form factors, in conjunction with the electromagnetic form factors, we can extract the strange quark contribution. The explicit dependence of the parity violating asymmetry on the strangeness content is written as follows in terms of the Sachs form factors introduced above, the neutral weak axial form factor G_A^{Zp} , the

Weinberg angle θ_W , Fermi constant G_F , fine-structure constant α , and kinematic factors Q^2 , τ , ϵ , and ϵ'

$$A^{\text{PV}} = -\frac{G_F|Q|^2}{4\pi\alpha\sqrt{2}} \times \rho' \left[(1 - 4\kappa' \sin^2 \theta_W) - \frac{\epsilon G_E^{\gamma p} (G_E^{\gamma n} + G_E^s) + \tau G_M^{\gamma p} (G_M^{\gamma n} + G_M^s) - 2\epsilon' (1 - 4 \sin^2 \theta_W) G_M^{\gamma p} G_A^{Zp}}{\epsilon (G_E^{\gamma p})^2 + \tau (G_M^{\gamma p})^2} \right] \quad (5)$$

The kinematic factors are $Q^2 = -q_\mu^2 > 0$, the square of the four-vector momentum transfer, $\tau = Q^2/4M^2$ where M is the proton mass, $\epsilon = [1 + 2(1 + \tau) \tan^2(\theta/2)]^{-1}$ where θ is the scattering angle, and $\epsilon' = \sqrt{\tau(1 + \tau)(1 - \epsilon^2)}$. The parameters $\rho' = 0.9879$ and $\kappa' = 1.0029$ arise from electroweak radiative corrections [47].

Note that the asymmetry also contains a term with the neutral weak axial form factor G_A^{Zp} which as explained in [46] can be estimated by combining information from neutron beta decay [47], polarized deep inelastic scattering [16], and calculations of the axial radiative correction [22, 48]; it is suppressed in the HAPPEX kinematics since $\epsilon' \sim 0.08$ and $1 - 4 \sin^2 \theta_W \sim 0.08$, and contributes only a few percent.

III. EXPERIMENTAL METHOD

A. Overview

The experiment measured the helicity-dependent left-right asymmetry in the scattering of longitudinally polarized 3.2 GeV electrons from a 15 cm long unpolarized liquid hydrogen target. Since the anticipated asymmetry was of the order of 10^{-5} or 10 parts per million (ppm), there were two characteristics that dictated the overall experimental design. First, the physical properties of the incident beam on target and the experimental environment as a whole had to be identical for the left- and right-handed beams to a very high degree so as to minimize spurious asymmetries. Second, in order to accumulate the required statistics at a high rate, the relative scattered flux was measured by integrating the response of the detector rather than by counting individual particles.

A GaAs photocathode was optically pumped by circularly polarized laser light to produce polarized electrons, with the ability to rapidly and randomly flip the sign of the electron

beam polarization. The asymmetry was extracted by generating the incident electron beam as a pseudorandom time sequence of helicity “windows” at 30 Hz and then measuring the fractional difference in the integrated scattered flux over window pairs of opposite helicity.

The elastically scattered electrons with $\theta_{\text{lab}} \sim 12.5^\circ$ were focused by two high-resolution spectrometers (HRS) onto detectors consisting of lead-lucite sandwich calorimeters. The Čerenkov light from each detector was collected by a photomultiplier tube, integrated over the duration of each helicity window and digitized by analog to digital converters (ADCs). The HRS pair has sufficient resolution to spatially separate the elastic electrons from inelastic electrons at the π^0 threshold. The amount of background was measured in separate calibration runs using conventional drift chambers, resulting in a small correction with negligible systematic errors.

The experiment was carefully designed to minimize the impact of random as well as of helicity-correlated fluctuations of the measured scattered flux. The electrical environment around the ADCs in particular and the data acquisition and control system as a whole were configured so that the observed fluctuations in the integrated scattered flux were dominated by counting statistics.

Apart from random jitter, an important class of potential false asymmetries might arise from helicity-correlated fluctuations in the physical properties of the beam, such as intensity, energy and trajectory. The helicity-correlated intensity asymmetry was maintained to be less than 1 ppm by an active feedback loop. The physical properties of the electron beam were monitored with high precision by beam monitors. The sensitivity of the scattered flux to fluctuations in the beam parameters was evaluated continuously and accurately by modulating judiciously placed corrector coils in the beam line leading to the hydrogen target. Separate data runs under different conditions determined that target density fluctuations were negligible for our kinematics.

The electron beam polarization was measured by three different techniques at varying intervals: Mott scattering, Møller scattering and Compton scattering. Figure 1 shows a schematic diagram of the important components of the HAPPEX experiment. In the following sections we elaborate on the above considerations in detail.

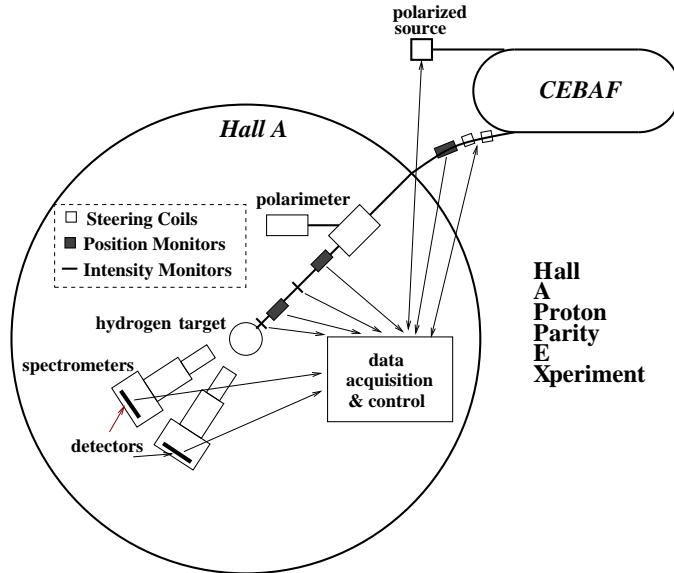


FIG. 1: Schematic Overview of the HAPPEX Experiment.

B. Polarized Electron Beam

1. The Polarized Source and Laser Optics

The longitudinally-polarized electron beam at Jefferson Lab is produced by illuminating a GaAs photocathode with circularly polarized laser light. For the 1998 run, a “bulk” GaAs photocathode was used, which delivered a beam intensity up to $100 \mu\text{A}$ with a polarization $\sim 38\%$. For the 1999 run, a “strained” GaAs photocathode was used, which produced a beam intensity of $\sim 40 \mu\text{A}$ with a polarization of $\sim 70\%$. This experiment was the first to use a strained GaAs photocathode to measure a parity-violating asymmetry in fixed-target electron scattering.

The source laser system provided laser light with the 1497 MHz microstructure of the JLab electron beam. A diagram of the source laser system is shown in Fig. 2. There were three lasers, which provided beams to the three different experimental halls, allowing individual control of beam intensities. Each laser system consisted of a gain-switched diode seed laser and a single-pass diode optical amplifier. Each seed laser was driven at 499 MHz, 120° out of phase with the others. The seed laser light was focused into a diode optical amplifier, whose respective drive current controllers allowed precise control of the beam intensity into each experimental hall.

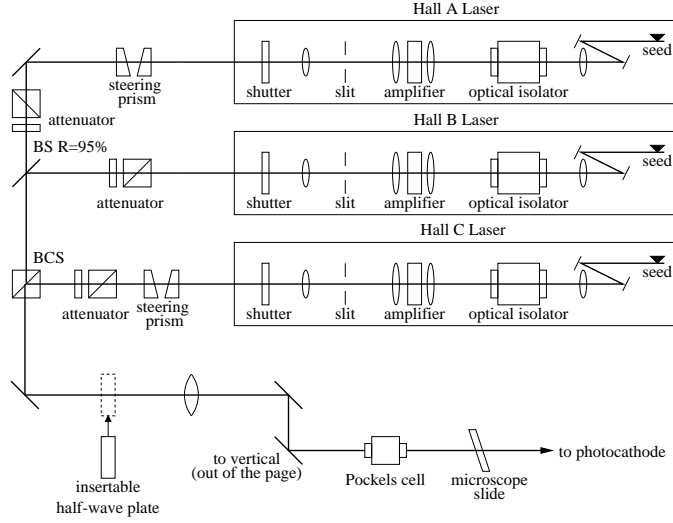


FIG. 2: Schematic diagram of the polarized source laser system showing the seed laser, diode amplifier, and components to steer, focus, and attenuate the beam and define its polarization. BS: beam splitter. BCS: beam combiner and splitter.

The Hall A laser light was guided through an attenuator consisting of a remotely rotatable half-wave plate and a linear polarizer, allowing a clean way to control the average beam intensity without affecting the properties of the diode amplifier. The three laser beams were then combined to produce the 1497 MHz pulse train. This beam was guided into a Pockels cell, which is essentially a voltage controlled retardation plate. The Pockels cell is configured to convert the linearly polarized light to right- or left-circularly polarized light. The polarity of the potential difference across the Pockels cell face determines the handedness of the laser beam at the exit of the cell.

Also shown in the figure are an insertable half-wave plate and a microscope slide. The half-wave plate is aligned with its fast axis at 45° with respect to the linear polarization of the laser beam, so that it rotates the incoming linear polarization by 90° , which in turn switches the handedness of the circular polarization exiting the Pockels cell. This was a powerful way of reversing the sign of the experimental asymmetry with minimal changes to the experiment. The microscope slide was used in conjunction with the feedback scheme to control the helicity-correlated intensity asymmetry. For the final phase of running with the “strained” photocathode, an additional half-wave plate was used downstream in order to control helicity-correlated position fluctuations. These details will be discussed in Sec. IV A.

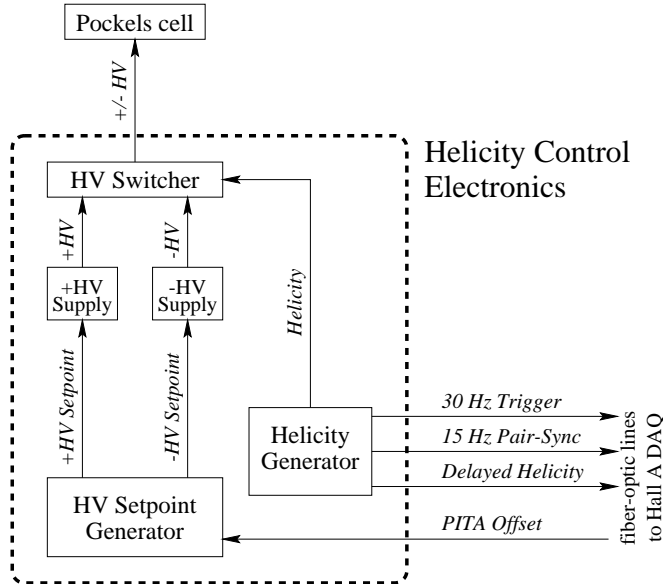


FIG. 3: Schematic diagram of the helicity control electronics. The *Helicity* signal drives the high voltage on the Pockels cell. The system is electrically isolated from the rest of the lab (dashed box).

2. *Helicity Control Electronics*

A schematic diagram of the helicity control electronics is shown in Fig. 3. The high voltage (HV) switcher provided the Pockels cell with positive or negative high voltage depending on the state of a digital control signal. The programmable HV supplies were set to correspond to $\pm\lambda/4$ retardation for the Pockels cell, which was approximately ± 2.5 kV. The net effect of the system was that the helicity of the electron beam depended on the state of the digital control signal, the *Helicity* signal.

The *Helicity* signal was provided by the Helicity Generator, a custom-built logic circuit which controlled the helicity sequence and timing structure of the polarization of the electron beam. As shown in the figure, the Helicity Generator also produced three other control signals that provided principal triggers to the data acquisition system.

The helicity of the beam was changed rapidly to minimize the possibility that slow drifts might bias the measured asymmetry. We chose to integrate over two 60 Hz cycles, setting the helicity every 33.33 ms. We denoted each 33 ms period of constant helicity as a “window”. Sensitivity to other, unforeseen frequencies was reduced by choosing the helicity using a

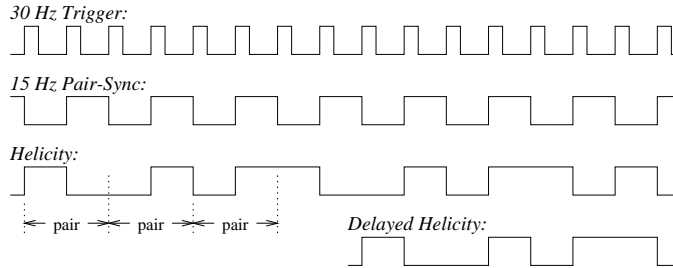


FIG. 4: Timing diagram of important control signals related to the beam helicity.

pseudo-random number generator sequence at 15 Hz. The helicity sequence was thus a train of “window pairs”: the helicity of the first window was chosen pseudo-randomly, while the second window was chosen to be the corresponding complement.

All signals to and from the Helicity Generator were routed via fiberoptic cable, thus allowing complete ground isolation of the helicity generator circuit from the rest of the experiment. This was a powerful way to reduce the possibility of helicity-correlated crosstalk and ground loops in the rest of the experiment, which could lead to spurious asymmetries. As a further precaution to suppress crosstalk, the true helicity of each window was fed into an 8-bit shift register, and the helicity that was transmitted to the data stream of the data acquisition system arrived 8 windows later, breaking any correlation with the helicity of the event. The timing signals described above are depicted in Fig. 4.

The system had one important input from the online analyzer of the data acquisition system: a DC level that allowed for small changes to the precise high voltages of the HV power supplies. This signal, labeled as “PITA offset” in Fig. 3, allowed for precise control of the helicity-correlated intensity asymmetry of the electron beam, and will be described in detail in section IV A 2. In order to preserve the ground isolation, the DC level was transmitted as a frequency over fiberoptic cable and then converted to an analog signal by a frequency-to-voltage converter.

C. Beam Fluctuations

The detected scattered flux D in each spectrometer, and the beam current I , were measured independently for every window. From these we obtained the normalized flux $d_i \equiv D_i/I_i$ and the cross section asymmetry $(A_d)_i$ for the i th window pair. The raw asym-

metry was then obtained by appropriate averaging of N measurements:

$$\begin{aligned} (A_d)_i &\equiv \left(\frac{d^+ - d^-}{d^+ + d^-} \right)_i \equiv \left(\frac{\Delta d}{2d} \right)_i \\ \delta(A_d) &= \sigma(A_d)/\sqrt{N}. \end{aligned} \tag{6}$$

where $+$ and $-$ denote the two helicity states in a pair. One goal of the experimental design was that $\sigma(A_d)$ should be dominated by the counting statistics in the scattered flux, greatly minimizing potential problems in the averaging procedure. As will be seen in Section VB, this goal was met. This is a result of the extraordinary characteristics of the electron beam and the associated beam instrumentation, which we discuss in this section.

The RMS noise in the asymmetry $\sigma(A_d)$ was found to be 3.8×10^{-3} at a beam current of approximately $100 \mu\text{A}$, which implied that roughly 70,000 electrons were recorded in the detectors during each beam window for a total rate of 2 MHz which was the expected rate and consistent with the rate extrapolated from lower currents. Since the experimental cross section is a function of the physical parameters of the beam, fluctuations in these parameters may contribute significantly to $\sigma(A_d)$. All electronic signals in the experiments are designed so that electronic noise is small compared to $\sigma(A_d)$.

There are two key parameters for each experimentally measured quantity M , such as detector rate, beam intensity *etc.* The first is $\sigma(\Delta M)$, the size of the relative window pair-to-window pair fluctuations in $\Delta M \equiv M_+ - M_-$, which is affected by real fluctuations in the electron flux. The second is $\delta(\Delta M)$, the relative accuracy with which the window pair differences in M can be measured compared to the true value, which is dominated by instrumentation noise.

If $\sigma(\Delta M)$ is large enough, it might mean that there are non-statistical contributions to $\sigma(A_d)$ so that the latter is no longer dominated by counting statistics. In this case, it is crucial that $\delta(\Delta M) \ll \sigma(\Delta M)$ so that window pair to window pair corrections for the fluctuations in ΔM can be made.

1. Random Fluctuations

As stated in III C, we desire that $\sigma(A_d)$ be dominated by counting statistics. An example of possible non-statistical contributions is window-to-window relative beam intensity fluctuations, $\sigma(A(I)) \equiv \sigma(\Delta I/2I)$, which were observed to vary between 2×10^{-4} and 2×10^{-3} ,

depending on the quality of the laser and the beam tune. This is remarkable and a unique feature of the beam at Jefferson lab, since $\sigma(A_I) < \sigma(A_d)$. Nevertheless, the detector-intensity correlation can be exploited to remove the dependence of beam charge fluctuations on the measured asymmetry:

$$(A_d)_i \simeq \left(\frac{\Delta D}{2D} - \frac{\Delta I}{2I} \right)_i \equiv (A_D - A_I)_i. \quad (7)$$

(This is equation 6 to first order.)

Similarly, $\sigma(A_d)$ might be affected by random beam fluctuations in energy, position and angle. The corrections can be parameterized as follows:

$$(A_d^{\text{corr}})_i = \left(\frac{\Delta D}{2D} - \frac{\Delta I}{2I} \right)_i - \sum_j (\alpha_j (\Delta X_j)_i). \quad (8)$$

Here, X_j are beam parameters such as energy, position and angle and $\alpha_j \equiv \partial D / \partial X_j$ are coefficients that depend on the kinematics of the specific reaction being studied, as well as the detailed spectrometer and detector geometry of the experiment.

By judicious choices of beam position monitoring devices (BPMs) and their respective locations, several measurements of beam position can be made from which the average relative energy, position, and angle of approach of each ensemble of electrons in a helicity window on target can be inferred. One can then write

$$(A_d^{\text{corr}})_i = \left(\frac{\Delta D}{2D} - \frac{\Delta I}{2I} \right)_i - \sum_j (\beta_j (\Delta M_j)_i). \quad (9)$$

Here M_i are a set of 5 BPMs that span the parameter space of energy, position, and angle on target, and $\beta_i \equiv \partial D / \partial M_i$. It is worth noting that this approach of making corrections window by window automatically accounts for occasional random instabilities in the accelerator (such as klystron failures) that are characteristic of normal running conditions.

During HAPPEX running, we found that $\sigma(\Delta M_j)$ varied between 1 and 10 μm and $\sigma(A_E)$ was typically less than 10^{-5} . These fluctuations were small enough that their impact on $\sigma(A_d)$ was negligible. Indeed, we believe that a significant contribution to the fluctuations in each monitor difference ΔM was the intrinsic measurement precision $\delta(\Delta M_i)$. We elaborate on this in section III C 2, where we discuss the monitoring instrumentation.

Another important consideration is the accuracy with which the coefficients β_i are measured. As mentioned earlier, these coefficients were evaluated using beam modulation, and will be discussed in Sect. IV B.

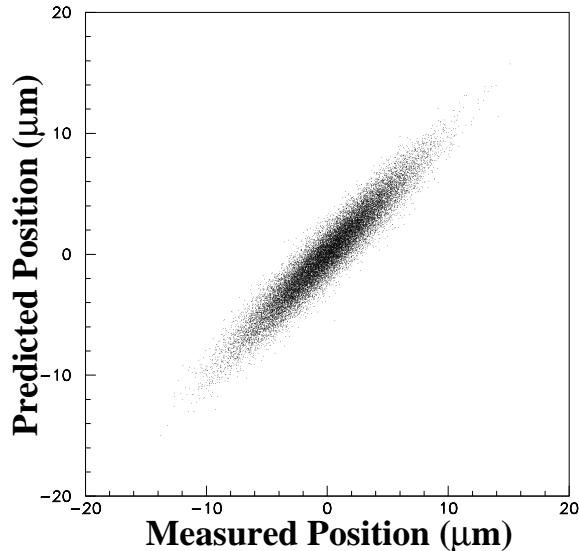


FIG. 5: Window-to-window beam jitter as measured by a BPM is plotted along the x axis. On the y axis is plotted the beam position as predicted by nearby BPMs. The residuals are smaller than $1 \mu\text{m}$.

2. Beam Monitoring

The above discussion regarding measurement accuracy and its impact on $\sigma(A_d)$ is particularly relevant in the monitoring of the electron beam properties such as beam intensity, trajectory and energy.

At Jefferson Lab, the beam position is measured by “stripline” monitors [49], each of which consists of a set of four plates placed symmetrically around the beam pipe. The plates act as antennae that provide a signal (modulated by the microwave structure of the electron beam) proportional to the beam position as well as intensity. Figure 5 shows the correlation between the measured position at a BPM near the target compared with the predicted position using neighboring BPMs for a beam current of $100 \mu\text{A}$ (2×10^{13} electrons per window). A precision for $\delta(\Delta X_i)$ close to $1 \mu\text{m}$ was obtained for the average beam position for a beam window containing 2×10^{13} electrons.

To measure the beam intensity, microwave cavity BCMs have been developed at Jefferson

Lab [50]. The precision $\delta(A_I)$ that has been achieved for a 30 ms beam window at 100 μA is 4×10^{-5} . This superior resolution is a result of good radiofrequency (rf) instrumentation as well as a high resolution 16-bit ADC, which will be discussed in section III G.

The absolute calibration of the beam current was performed with a parametric current transformer, the ‘Unser monitor’ [51]. Although the absolute calibration was not important for HAPPEX, the Unser monitor was useful to establish the pedestals and understand the linearity of the cavity current monitors.

3. Systematic Fluctuations

Assuming that $\sigma(A_d)$ has negligible contributions from window-to-window beam fluctuations and instrumentation noise, there is still the possibility that there are helicity-correlated systematic effects at the sub-ppm level. If one considers the cumulative corrected asymmetry A_d^{corr} over many window pairs, one can write

$$\begin{aligned} A_d^{\text{corr}} &\equiv \langle (A_d^{\text{corr}})_i \rangle = \\ &\quad \left\langle \left(\frac{\Delta D}{2D} \right)_i \right\rangle - \left\langle \left(\frac{\Delta I}{2I} \right)_i \right\rangle - \sum_j \beta_j \langle (\Delta M_j)_i \rangle \\ &= A_D - A_I - \sum_j A_{Mj}. \end{aligned} \tag{10}$$

For most of the running conditions during data collection, $A_d^{\text{corr}} \simeq A_D \simeq 10$ ppm, which meant that all corrections were negligible. The cumulative average for A_I was maintained below 0.1 ppm. For A_{Mj} , the cumulative averages were found to be below 0.1 ppm during the run with the ‘‘bulk’’ GaAs photocathode. This resulted from the fact that the accelerator damped out position fluctuations produced at the source by a large factor (section IV A 4). The averaged position differences on target were kept below 10 nm.

However, during data collection with ‘‘strained’’ GaAs, position differences as large as several μm were observed in the electron beam at a point in the accelerator where the beam energy is 5 MeV. Continuous adjustment of the circular polarization of the laser beam was required to reduce the differences to about 0.5 μm . This resulted in observed position differences on target ranging from 10 nm to 100 nm, which in turn resulted in A_{Mj} in the range from 0.1 to 1 ppm.

The control of the asymmetry corrections within the aforementioned constraints was one of the central challenges during data collection. A variety of feedback techniques on the laser

and electron beam properties were employed in order to accomplish this; these methods are discussed in Sec. IV A.

D. Target

The Hall A cryogenic target system [50] was used for this experiment. The target system consists of three separate cryogenic target loops in an evacuated scattering chamber, along with subsystems for cooling, temperature and pressure monitoring, target motion, gas-handling, controls, and a solid and dummy target ladder. Of the three cryogenic loops (hydrogen, deuterium, and helium), only the hydrogen loop was used in this experiment and will be described here. The hydrogen loop has two separate target cells, of 15 cm and 4 cm in length, respectively; only the 15 cm cell was used here.

The liquid hydrogen loop was operated at a temperature of 19 K and a pressure of ~ 26 psia, leading to a density of about 0.0723 g/cm^3 . The Al-walled target cells were 6.48 cm in diameter, and were oriented horizontally, along the beam direction. The upstream window thickness was 0.071 mm, the downstream window thickness was 0.094 mm, and the side wall thickness was 0.18 mm. Also mounted on the target ladder were solid thin targets of carbon, and aluminum dummy target cells, for use in background and spectrometer studies.

The target was mounted in a cylindrical scattering chamber of 104 cm diameter, centered on the pivot for the spectrometers. The scattering chamber was maintained under a 10^{-6} torr vacuum. The spectrometers view exit windows in the scattering chamber that were made of 0.406 mm thick Al foil.

The target coolant, ^4He gas at 15 K, was provided by the End Station Refrigerator (ESR), with a flow rate controlled using Joule-Thompson valves, which could be adjusted either locally or remotely. At the beam currents used here (up to $100 \mu\text{A}$) the beam heating load was of order 600 W. Including the heating from the target circulation fans, and a small ($\sim 45 \text{ W}$) target heater, the load could reach 1 kW, which could be adequately supplied by the ESR. In addition to the 45 W target heater, used in a feedback system in order to stabilize the target temperature, a high power heater (up to 1 kW) was automatically switched on when the beam dropped out suddenly. This target has achieved a luminosity of $5 \times 10^{38} \text{ cm}^{-2}\text{s}^{-1}$.

The target temperature was monitored continuously using 1) radiation hard

semiconductor-based sensors, Lakeshore CERNOX [52], 2) Allen-Bradley resistive sensors [53], and 3) vapor-pressure transducers. The temperature control system was computer controlled using a PID (proportion, integral and derivative) feedback system. The control system was based on the EPICS [54] system.

The normal electron beam spot size of about $50\ \mu\text{m}$ is small enough to potentially damage the target cells at full beam current, as well as to cause local boiling in the target even at reduced currents. A beam rastering system was used to distribute the heat load throughout the target cell. The beam was rastered at 20 kHz by two sets of steering magnets 23 m upstream of the target. These magnets deflected the beam by up to $\pm 2.5\ \text{mm}$ in x and y at the target. For the 1998 run, a rectangular raster pattern was used, while for the 1999 run a helical pattern was adopted, which provided a more uniform distribution of heat load. Local target boiling would manifest itself as an increase in fluctuations in the measured scattering rate, which would lead to an increase in the standard deviation of the pulse-pair asymmetries in the data, above that expected from counting statistics. Studies of the pulse-pair asymmetries for various beam currents and raster sizes were performed, at a lower Q^2 and thus at a higher scattering rate. Figure 6 shows the standard deviation of the pulse-pair asymmetries, extrapolated to full current values, for various beam currents and raster sizes. A significant increase over pure counting statistics, indicating local boiling effects, was observed only for the combination of a small raster (1.0 mm) size and large beam current ($94\ \mu\text{A}$). During the experiment we used larger raster sizes for which there was little boiling noise.

E. High Resolution Spectrometers in JLab Hall A

The Hall A high resolution spectrometers (HRS) at Jefferson Lab consist of a pair of identical spectrometers of QQDQ design, together with detectors for detecting the scattered particles [50]. For HAPPEX, the spectrometer and their standard detector package served the following purposes: 1) to suppress background from inelastics and low-energy secondaries; 2) to study the backgrounds in separate runs at or near the HAPPEX kinematics; 3) to measure the momentum transfer Q^2 ; 4) to measure and monitor the attenuation in the HAPPEX detector through the use of tracking; and 5) to measure the detector amplitude weighting factors for fine bins in Q^2 (section VI C).

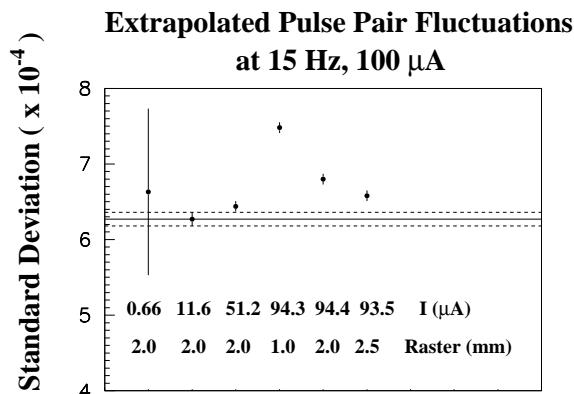


FIG. 6: Noise in pulse pair asymmetries vs. beam current and raster size. The width of asymmetries is extrapolated to 15 Hz, 100 μ A to check if it is consistent (within the dashed bars) with expectation. A value above this indicates target density fluctuations that increase the noise. For reasonably large raster patterns we saw little noise at 94 μ A.

The spectrometers are designed to have a large acceptance with excellent resolution and absolute accuracy in the reconstructed four-vectors of the events and, of less relevance for HAPPEX, precise normalization of the cross section. The momentum resolution is necessary for HAPPEX to separate the elastically scattered electrons from inelastic background, thus allowing the integrating technique. To measure Q^2 with sufficient accuracy requires good knowledge of the transfer matrix for the spectrometer to reconstruct events at the scattering point, as well as good pointing accuracy for the location of the spectrometers and precise measurements of beam position and angle. The achieved properties of the HRS are listed in Table I. The spectrometer detector package include scintillators for triggering and vertical drift chambers for reconstruction of particle trajectories, in addition to Čerenkov and lead glass detectors for particle identification. The trigger is formed in programmable CAMAC electronics and is configurable to include various combinations of the scintillator and other detectors including the HAPPEX detector (see section III F).

TABLE I: **Properties of the Hall A Spectrometers**

Magnet Configuration	QQDQ
Luminosity	$10^{38} \text{ cm}^{-2} \text{ sec}^{-1}$
Momentum Range (spectrometer 1)	0.2 - 4.3 GeV/c
Momentum Range (spectrometer 2)	0.2 - 3.2 GeV/c
Bend Angle	45°
Optical Length	23.4 m
Dispersion	12.4 cm/%
Momentum Acceptance	$\pm 4.5\%$
Momentum Resolution (FWHM)	2×10^{-4}
Solid Angle Acceptance	6 msr
Horizontal Angle Acceptance	$\pm 28 \text{ mrad}$
Vertical Angle Acceptance	$\pm 60 \text{ mrad}$
Target Length Acceptance (90°)	10 cm
Transverse Position Resolution (FWHM)	1.5 mm
Missing Energy Resolution (FWHM)	1.3 MeV

F. Focal Plane Detector

A total absorption shower counter was located in the focal plane of each spectrometer to detect the elastically scattered electrons. These detectors were based on a layered lead-acrylic geometry. Čerenkov light in the shower propagates along the acrylic and is detected at one end using a single photomultiplier tube (PMT); see Fig. 7.

These simple focal plane detectors were chosen over, for example, lead glass, because of their superior resistance to radiation damage. The radiation dose expected per detector was approximately 40 Gy in a 30 day data-taking run, which would cause significant decrease in optical transmission for a lead glass detector. Acrylic is significantly less susceptible to radiation damage. The insensitivity of such a detector to low-energy backgrounds was also an important design criterion.

The detectors were made up of 4 layers of 6.4 mm thick lead sheets sandwiched between 5 layers of 1.27 cm thick acrylic (Bicron BC-800 UVT Lucite). Each layer of acrylic was

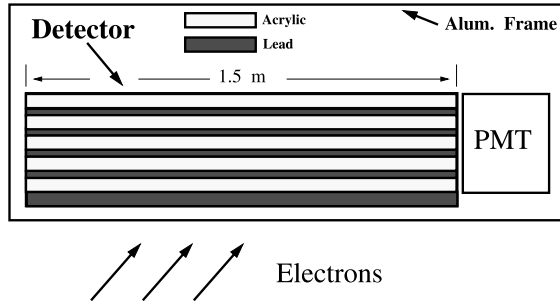


FIG. 7: Schematic of the focal plane detector. The scattered electrons strike a lead-acrylic shower counter whose light is collected by a PMT and integrated over a helicity period.

wrapped with a Teflon sheet, which does not adhere to the surface, thereby preserving internal reflection from the acrylic-air interface. The incident electrons first passed through a 1.9 cm Teflon spacer and 2 layers of 6.4 mm lead sheets acting as a pre-radiator. The segmentation was chosen in order to provide a sufficiently good energy resolution ($15\% \sigma$) with the use of commercially available thicknesses of acrylic while maintaining mechanical simplicity. The detector energy resolution affects the error on the physics asymmetry via

$$\delta A \sim \frac{1}{\sqrt{N}} \sqrt{1 + \left(\frac{\Delta E}{\langle E \rangle} \right)^2} \quad (11)$$

where N is the number of window pairs, ΔE is the energy resolution of the detector, and $\langle E \rangle$ is the average detected energy. The width (10 cm) and length (150 cm) of the sandwich stack was chosen in order to contain the entire image of the elastically scattered electrons in the focal plane, as well as much of the radiative tail, and yet not detect events from inelastic scattering. The width of the distribution of elastic events on the focal plane was 3 cm, so edge effects were small.

The detector sandwich was viewed at one end by a single 12.7 cm diameter Burle 8854 photomultiplier tube. A pair of blue LEDs was mounted in the middle acrylic layer, at the opposite end from the PMT, for use in study of detector linearity and attenuation. Tests using the LEDs indicated that the non-linearity of the detector was less than 1.5% at typical operating voltages.

Bench tests of the detectors using cosmic rays showed that the signal output was a strong

function of the incident particle's position along the detector's length, due primarily to bulk absorption of light in the acrylic. While the Bicron BC-800 UVT Lucite acrylic is transparent to wavelengths shorter than for ordinary acrylic, it has a strong attenuation for wavelengths shorter than about 350 nm. Given that the PMT used has significant sensitivity down to 250 nm, and given the short wavelengths of typical Čerenkov light, the bulk attenuation in the acrylic led to a measured decrease in the light output of 50%/m. To decrease this attenuation, a single sheet of Plexiglass was installed directly in front of the PMT to filter out the UV light. After installation of this filter the dependence of light output on position along the detector was reduced to 9%/m, at the cost of a reduction in the total gain, which was acceptable for this experiment.

The detector, as expected, also exhibited a strong sensitivity to the angle of the incident particles, with a maximum output when the angle was such that part of the Čerenkov cone pointed directly at the PMT (see Fig. 8). This angular sensitivity was an advantage. Since the elastic electrons arrive at the focal plane at well-known angles, the detector orientation can then be adjusted to maximize the sensitivity to the elastically scattered events while minimizing the sensitivity to backgrounds that arrive at other angles.

Due to the optics of the spectrometer, the incident angle of the elastically-scattered electrons varies with their position along the detector's length. Thus the crossing angle sensitivity leads to an additional variation of the detector's response with position along the detector. The total effect of variation along the detector position was measured periodically during data-taking and was $(17.3 \pm 0.5)\%/m$. This value was stable during the run, indicating no significant degradation of the optical properties of the detector due to radiation damage.

The detector was mounted in a light-tight aluminum box with 1 cm thick walls and was supported over the vertical drift chambers in a frame that allowed adjustment of the horizontal location, as well as the pitch, roll and yaw angle of the detector. The detector's strong sensitivity to the incident angle of the incoming electron necessitated the ability to orient the detector precisely. All material used in the detector box and support frame near the active region was chosen to be non-ferric in order to reduce the possibility of false asymmetries due to Møller scattering of electrons off magnetized material. More information on the detectors is available in [8].

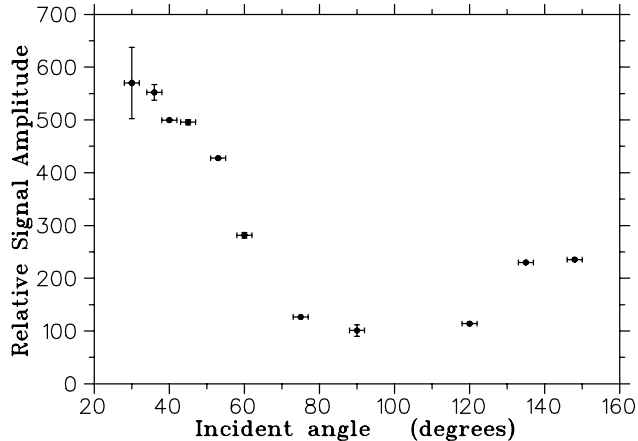


FIG. 8: Focal plane detector response versus angle of incident particle with respect to the long axis of the focal plane detector, measured using cosmic rays.

G. Data acquisition and Custom ADCs

Signals from the various detectors and monitors are integrated and digitized by custom-built VME integrating ADCs in a data acquisition system (DAQ) based on the CODA DAQ package [55] triggered at nominally 30 Hz, synchronized to the end of each helicity window. In addition to these ADCs, the DAQ reads scalers and input/output registers which count various information such as helicity pulses.

The custom ADCs integrate the data over most of the 33 msec helicity pulse. The first 0.5 msec of the pulse is blanked off to remove instabilities due to the switching of HV on the Pockels cell which controls the beam polarization. The ADCs are designed to achieve high resolution (16 bits) with low differential nonlinearity ($\leq 0.1\%$). Each ADC channel (Fig. 9) consists of an input amplifier, an integrating circuit, two sample-and-hold circuits, a difference amplifier, a summing circuit, and a 16 bit ADC chip. The input amplifier converts the input voltage to a scaled current which is integrated in the next stage; for current signals such as PMTs this amplifier stage is bypassed and the signal is integrated directly. The integrator output is sampled and held once 700 μ sec after the beginning of the helicity pulse, and again 32 msec later near the end of the pulse. The difference between these two is the integrated result. The circuit components were chosen to emphasize low noise at the expense of speed. Noise widths of 3 ADC channels FWHM have been achieved.

To achieve the nonlinearity specification, a pseudorandom DAC voltage (“DAC noise”) is added to the integrated result prior to digitization by the ADC, then subtracted later in

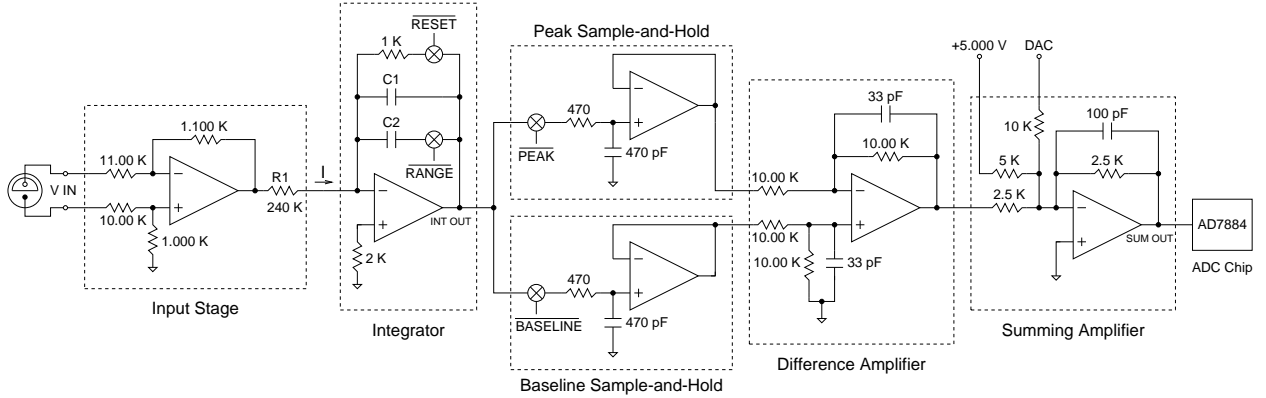


FIG. 9: Circuit diagram of one channel of the custom 16 bit integrating ADC.

analysis. DAC noise solves a problem of nonlinearity that arises generally in the digitization of data which leads to a systematic error in the asymmetry that can be estimated as follows. Consider a signal of average value S (ADC channels) and RMS width σ , and let the deviation from ideal linear response be denoted D which is typically the least count bit. Denote the helicity correlated asymmetry in the signal by A . Then if $AS \ll \sigma$ the relative systematic error in the asymmetry will be $dA/A \approx KD/\sigma$ with $K \simeq 1$. (For Gaussian signals $K = 2/\sqrt{2\pi}$.) Thus, the DAC noise smears the data over many ADC channels, which reduces systematic errors from bit resolution. Since the noise is later subtracted it does not increase the statistical error.

The data acquisition software is based on the CODA 1.4 package [55]. The trigger interrupt service routine in the VME controller assembles the following data into an event record: ADC data, ADC flags, scaler data, trigger controller data, VME flags, beam modulation data, and Pockels cell high voltage offsets. The ADC data include the digitized ADC outputs and the value of the DAC noise that had been added to the ADC signal. The ADC flags govern various options for each ADC board. Data from the trigger controller include a flag indicating the helicity of the first window of the pair, and a flag indicating whether the window is the first or the second of a pair. As described in section III B 2, the helicity flag is delayed at the polarized source and applies to the eighth window preceding the one with which it is collected. The VME flags govern various options for the VME controller. Beam modulation data describe the state of the beam modulation system including the object being modulated, the size of its offset, and flags indicating whether the object's state was stable during the event.

The complete event record is then sent over the network to the data acquisition workstation, where the data files are written to disk and are processed by an online analyzer.

A separate process on the VME controller is able to handle requests via a TCP/IP socket to change or report various system parameters, including the ADC and VME flags, beam intensity feedback parameters, and the Pockels cell high voltage offset, and to enable or disable the beam modulation system.

The online analyzer verifies the integrity of the data, determines where cuts due to beam off or computer dead time are required, associates the delayed helicity information with its proper window, groups windows into opposite-helicity pairs, subtracts DAC noise from each ADC signal, computes x and y positions from the BPM data, and packages the data into files in the PAW ntuple format for further analysis.

Another function of the online analyzer is to handle beam intensity feedback. Beam intensity asymmetries are averaged over a user-defined interval, typically 2500 pairs, termed a “minirun”. At the end of each minirun the change to the Pockels cell high voltage offset required to null the observed intensity asymmetry is computed. The analyzer then issues a request for the VME controller to make the appropriate change to the offset.

H. Polarimetry

The experimental asymmetry A^{exp} is related to the corrected asymmetry by

$$A^{\text{exp}} = A_d^{\text{corr}}/P_e \quad (12)$$

where P_e is the beam polarization. Three beam polarimetry techniques were available at JLab for the HAPPEX experiment: A Mott polarimeter in the injector, and both a Møller and a Compton polarimeter in the experimental hall.

1. Mott Polarimeter

A Mott polarimeter [57] is located near the injector to the first linac, where the electrons have reached 5 MeV in energy. Mott polarimetry is based on the scattering of polarized electrons from unpolarized high-Z nuclei. The spin-orbit interaction of the electron’s spin with the magnetic field it sees due to its motion relative to the nucleus causes a differential

cross section

$$\sigma(\theta) = I(\theta) \left[1 + S(\theta) \vec{P}_e \cdot \hat{n} \right] , \quad (13)$$

where $S(\theta)$, known as the Sherman function, is the analyzing power of the polarimeter, and $I(\theta)$ is the spin-averaged scattered intensity

$$I(\theta) = \frac{Z^2 e^4}{4m^2 \beta^4 c^4 \sin^4(\theta/2)} [1 - \beta^2 \sin^2(\theta/2)] (1 - \beta^2) . \quad (14)$$

The unit vector \hat{n} is normal to the scattering plane, defined by $\hat{n} = (\vec{k} \times \vec{k}') / |\vec{k} \times \vec{k}'|$ where \vec{k} and \vec{k}' are the electron's momentum before and after scattering, respectively. Thus $\sigma(\theta)$ depends on the electron beam polarization P_e . Defining an asymmetry

$$A(\theta) = \frac{N_L - N_R}{N_L + N_R} , \quad (15)$$

where N_L and N_R are the number of electrons scattered to the left and right, respectively, we have

$$A(\theta) = P_e S(\theta) , \quad (16)$$

and so knowledge of the Sherman function $S(\theta)$ allows P_e to be extracted from the measured asymmetry.

The 5 MeV Mott polarimeter employs a 0.1 μm gold foil target, and four identical plastic scintillator total-energy detectors, located symmetrically around the beam line at a scattering angle of 172° , the maximum of the analyzing power. This configuration allows a simultaneous measurement of the two components of polarization transverse to the beam momentum direction. A Wien filter upstream of the polarimeter is used to rotate the electron's spin from longitudinal to transverse polarization for the Mott measurement. Multiple scattering in the foil target leads to substantial uncertainty in the analyzing power which is evaluated by measurements for a range of target foil thicknesses and an extrapolation to zero thickness. It is believed [56] that the theoretically calculated single-atom analyzing power (Sherman function) is the correct number to use for zero target thickness extrapolation. The primary systematic errors of the device were the extrapolation to zero target foil thickness (5% relative) and background subtraction (3%) [57], see section VIA 1.

2. Møller Polarimeter

A Møller polarimeter measures the beam polarization via measuring the asymmetry in \vec{e}, \vec{e} scattering, which depends on the beam and target polarizations P^{beam} and P^{target} , as well as on the analyzing power A_m^{th} of Møller scattering:

$$A_m^{\text{exp}} = \sum_{i=X,Y,Z} (A_{mi}^{\text{th}} \cdot P_i^{\text{target}} \cdot P_i^{\text{beam}}), \quad (17)$$

where $i = X, Y, Z$ defines the projections of the polarizations (Z is parallel to the beam, while $X - Z$ is the scattering plane). The analyzing powers A_{mi}^{th} depend on the scattering angle θ_{CM} in the center-of-mass (CM) frame and are calculable in QED. The longitudinal analyzing power is

$$A_{mZ}^{\text{th}} = -\frac{\sin^2 \theta_{\text{CM}} (7 + \cos^2 \theta_{\text{CM}})}{(3 + \cos^2 \theta_{\text{CM}})^2}. \quad (18)$$

The absolute values of A_{mZ}^{th} reach the maximum of $7/9$ at $\theta_{\text{CM}} = 90^\circ$. At this angle the transverse analyzing powers are $A_{mX}^{\text{th}} = -A_{mY}^{\text{th}} = A_{mZ}^{\text{th}}/7$.

The polarimeter target is a ferromagnetic foil magnetized in a magnetic field of 24 mT along its plane. The target foil can be oriented at various angles in the horizontal plane providing both longitudinal and transverse polarization measurements. The asymmetry is measured at two target angles ($\pm 20^\circ$) and the average taken, which cancels transverse contributions and reduces the uncertainties of target angle measurements. At a given target angle two sets of measurements with oppositely signed target polarization are made which cancels some false asymmetries such as beam current asymmetries. The target polarization was $(7.95 \pm 0.24)\%$.

The Møller-scattered electrons were detected in a magnetic spectrometer (see Fig. 10) consisting of three quadrupoles and a dipole [50].

The spectrometer selects electrons in a bite of $75^\circ \leq \theta_{\text{CM}} \leq 105^\circ$ and $-5^\circ \leq \phi_{\text{CM}} \leq 5^\circ$ where ϕ_{CM} is the azimuthal angle. The detector consists of lead-glass calorimeter modules in two arms to detect the electrons in coincidence. More details about the Møller polarimeter are published in [50]. The total systematic error that can be achieved is 3.2% which is dominated by uncertainty in the foil polarization.

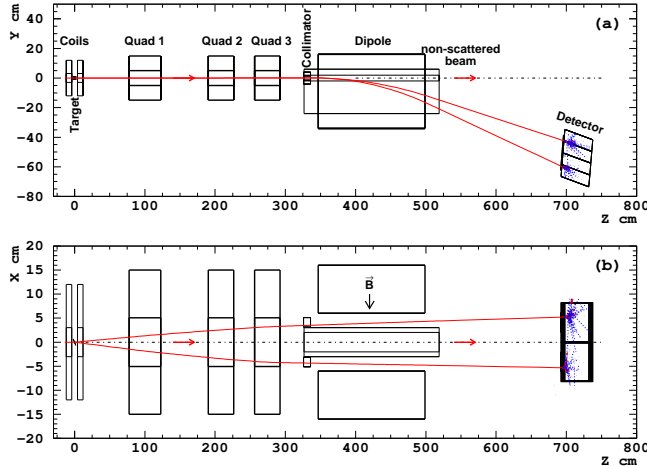


FIG. 10: Layout of the Hall A Møller polarimeter.

3. Compton Polarimeter

The Compton polarimeter performed its first measurements during the second HAPPEX run in July 1999 [58]. It is installed on the beam line of Hall A (see Fig.11). The electron beam interacts with a polarized “photon target” in the center of a vertical magnetic chicane that aims at separating the scattered electrons and photons from the primary beam. The backscattered photons are detected in a matrix of 25 $PbWO_4$ crystals [59].

The experimental asymmetry $A_c^{\text{exp}} = (N^+ - N^-)/(N^+ + N^-)$ is measured, where N^+ (N^-) refers to Compton counting rates for right (left) electron helicity, normalized to the beam intensity. This asymmetry is related to the electron beam polarization via

$$P_e = \frac{A_c^{\text{exp}}}{P_\gamma A_c^{\text{th}}} \quad (19)$$

where P_γ is the photon polarization and A_c^{th} the analyzing power. At typical JLab energies (a few GeV), the Compton cross-section asymmetry is only a few percent. An original way to compensate this drawback is the implementation of a Fabry-Perot cavity [60] which amplifies the photon density of a standard low-power laser at the integration point. An average power of 1200 W is accumulated inside the cavity with a photon beam waist of the order of 150 μm and a photon polarization above 99%, monitored online at the exit of the cavity [61].

Since less than 10^{-9} of the beam undergoes Compton scattering, and thanks to the zero total field integral of the magnetic chicane, the primary beam is delivered unchanged to the

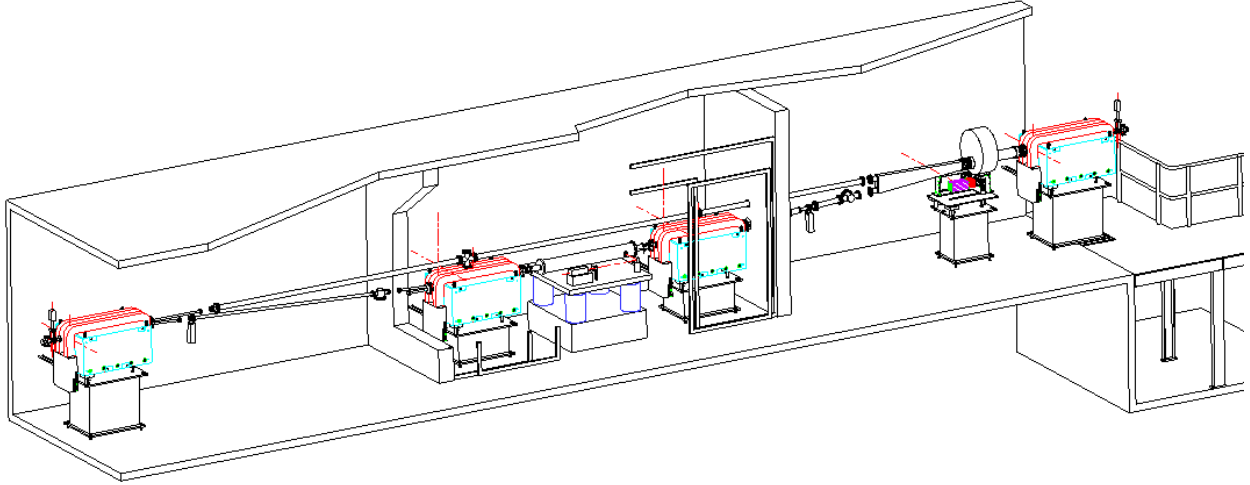


FIG. 11: Oblique view of the Compton polarimeter. The beam enters from the left and is bent down into a chicane where it intersects the laser cavity. The cavity is on the bench in the middle of the chicane. The photon detector for backscattered photons is on the bench just upstream of the last chicane magnet.

experimental target. These features make Compton polarimetry an attractive alternative to other techniques, as it provides a non-invasive measurement simultaneous with the running experiment.

The quality of the polarization measurement is driven by the tuning of the electron beam in the center of the magnetic chicane. In the early tests a large background rate was generated in the photon detector by the halo of the electron beam scraping on the narrow apertures of the ports in the mirrors of the cavity. Extra focusing in the horizontal plane, induced by an upstream quadrupole dramatically reduces this background. Then a fine adjustment of the electron beam vertical position optimizes the luminosity at the Compton interaction point. Figure 12 illustrates that beyond maximizing the luminosity, standing near the optimum position also reduces our sensitivity to electron beam position differences correlated with the helicity.

In the data-taking procedure, periods of cavity ON (resonant) and cavity OFF (unlocked) are alternated in order to monitor the background level and asymmetry. A typical signal over background ratio of 5 is achieved and the associated errors are small.

The photon polarization is reversed for each ON period, reducing the systematic errors

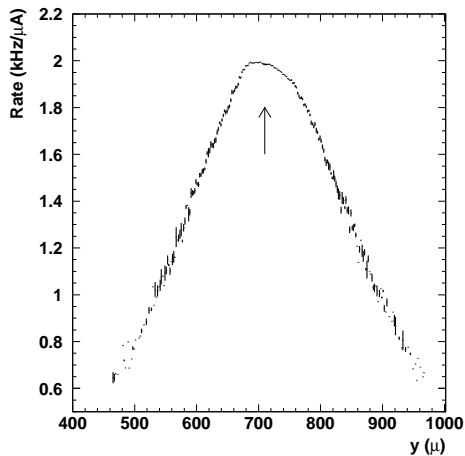


FIG. 12: Counting rate normalized to beam current versus vertical position of the electron beam for the Compton polarimeter. The sensitivity to beam position differences is proportional to the derivative of this curve. The arrow points to where we run.

due to electron helicity correlations. These correlations are already minimized by our controls at the source (see Sec. IV A). By summing the Compton asymmetries of the right and left photon polarization states with the proper statistical weights we expect the effects of helicity correlations to cancel out to first order and the residual effects to be small. Nevertheless, extra slow drifts in time of the beam parameters can occur and increase the sensitivity to helicity correlations. In order to select stable running conditions we apply cuts of $\pm 3 \mu A$ on the beam current and reject all the coil-modulation periods in the analysis. This leads to the loss of 1/3 of the events. In the end the residual helicity correlated luminosity asymmetry A_F still contributed 1.2% to the experimental Compton asymmetry and remained its main source of systematic error (cf. Table II).

An optical setup allows us to monitor the photon polarization at the exit of the cavity. The connection with the “true” polarization P_γ at the Compton interaction point is given by a transfer function measured once during a maintenance period. Polarizations for right and left handed photons are found to be stable in time and given by $P_\gamma^{R,L} = \pm 99.3_{-1.1}^{+0.7}\%$.

The last ingredient of Eq. 19 is the analyzing power A_c^{th} . The response function of the photon detector (see Fig. 13) is parametrized by a Gaussian resolution $g(k')$ of width

$$\sigma_{\text{res}}(k') = \sqrt{a + \frac{b}{k'} + \frac{c}{(k')^2}}, \quad (20)$$

TABLE II: Average relative error budget for the beam polarization measured using the Compton polarimeter, based on 40 measurements in the 1999 run. S and B refer to signal and background, A_B is the asymmetry in the background, and A_F is the helicity correlated luminosity asymmetry.

Source	Systematic		Statistical
P_γ		1.1%	
A_c^{exp}	Statistical		1.4%
	B/S	0.5%	
	A_B	0.5%	1.4%
	A_F	1.2%	
A_c^{th}	Non-linearities	1%	
	Calibration	1%	
	Efficiency/Resolution	1.9%	2.4%
Total	3.3%		

where k' is the backscattered photon energy. A Gaussian was used because the complete study of the calorimeter response wasn't available at the time of this analysis; the corresponding errors in the calibration, efficiency, and resolution are shown in Table II and explained here. The coefficients (a, b, c) are fitted to the data (Fig. 13). A “smeared” cross section is then obtained

$$\frac{d\sigma_{\text{smeared}}^\pm}{dk'_r} = \int_0^\infty \frac{d\sigma_c^\pm}{dk'} g(k' - k'_r) dk' \quad (21)$$

where k'_r is the energy deposited in the calorimeter and $d\sigma_c^\pm/dk'$ the helicity-dependent Compton cross section. Experimentally, the energy spectrum has a finite width at the threshold (see Fig. 13) which is modeled by an error function $p(k'_s, k'_r) = \text{erf}((k'_r - k'_s)/\sigma_s)$ where σ_s is fitted to the data as well. This width can be due either to the fact that the threshold level itself is unstable, or to the fact that a given k'_r can correspond to different voltages at the discriminator level.

Finally, the observed counting rates can be expressed as

$$N^\pm(k'_s) = L \times \int_0^\infty p(k'_s, k'_r) \frac{d\sigma_{\text{smeared}}^\pm}{dk'_r} dk'_r \quad (22)$$

where L stands for the interaction luminosity and the analyzing power of the polarimeter

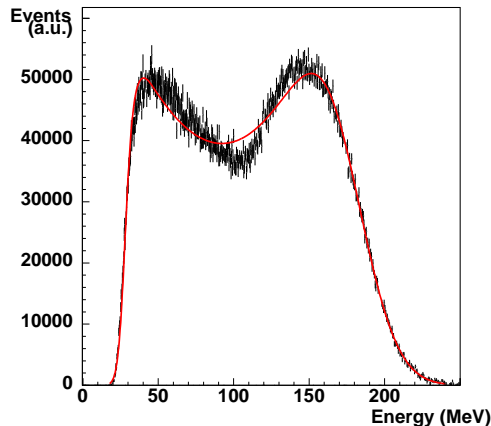


FIG. 13: Compton spectrum as measured by the photon calorimeter. The curve is a fit of the Compton cross-section convoluted with a Gaussian resolution of the calorimeter (see Eq. 20).

can be calculated as

$$A_c^{\text{th}} = \frac{N^+(k'_s) - N^-(k'_s)}{N^+(k'_s) + N^-(k'_s)} \quad (23)$$

The analyzing power is of the order of 1.7%. To estimate the systematic error in the modeling of the calorimeter response, we varied the parameters a , b , c , k'_s , and σ_s around their fitted values. The sizes of those variations were chosen to reproduce the dispersion of the experimental data. The analyzing power was then computed for each of the possible combinations of the cross variations of the five parameters and the maximum deviation from the nominal analyzing power was assigned as the systematic error. This contributed a systematic error of 1.9 % [62].

Other systematic errors related to non-linearities in the electronics and uncertainty in the energy calibration, which is performed by fitting the Compton edge, make only a small contribution to the final error (cf. table II). Further information on the Compton polarimeter is available in [58].

IV. SYSTEMATIC CONTROL

A. Control of the Laser Light

Section III B 1 describes the optics of the polarized electron source. Here, we discuss how those optics were used to control the laser beam's polarization and to suppress helicity-

correlated beam asymmetries.

1. Laser Polarization and the PITA Effect

The Pockels cell that is used to circularly polarize the laser beam acts as a voltage-controlled quarter-wave plate. Depending on the sign of the voltage applied to it, it can produce light of either helicity. The Pockels cell is an imperfect quarter-wave plate, however, and a convenient way to parameterize the phase shift it induces on the laser beam is

$$\delta_R = -\left(\frac{\pi}{2} + \alpha\right) - \Delta, \quad \delta_L = +\left(\frac{\pi}{2} + \alpha\right) - \Delta, \quad (24)$$

where δ_R (δ_L) is the phase shift induced by the Pockels cell to produce right- (left) helicity light. The imperfections in the phase shift are given by α (“symmetric” offset) and Δ (“antisymmetric” offset), and perfect circular polarization is given by the condition $\alpha = \Delta = 0$. When an imperfectly circularly polarized laser beam is incident on an optical element that possesses an analyzing power (as in Fig. 14), an intensity asymmetry results that depends on the antisymmetric phase, Δ . To first order, this intensity asymmetry can be expressed as

$$A = -\frac{\epsilon}{T} \cos 2\theta \cdot (\Delta - \Delta^0), \quad (25)$$

where the ratio $\epsilon/T \ll 1$ is the “analyzing power” of the optical element defined in terms of the difference in optical transmission fractions between two orthogonal axes (x' and y' in fig 14), $\epsilon = T_{x'} - T_{y'}$, divided by the summed transmission fractions $T = T_{x'} + T_{y'}$, and θ is the angle between the Pockels cell’s fast axis and the x' transmission axis of the analyzer, and Δ^0 is an offset phase shift introduced by residual birefringence in the Pockels cell and the optics downstream of it. This effect is referred to as the Polarization-Induced Transport Asymmetry (PITA) effect [63, 64] and was one of the dominant sources of helicity-correlated beam asymmetries. The intensity asymmetry is proportional to Δ , and the constant of proportionality $(\epsilon/T) \cos 2\theta$ is referred to as the “PITA slope”. Any optical element downstream of the Pockels cell possesses a small analyzing power. For the 1998 run, a glass slide was introduced into the laser beam to provide a small controlled analyzing power. For the 1999 run, the QE anisotropy of the strained GaAs cathode (which behaves in this case in a manner formally equivalent to an optical analyzing power) acted as the dominant source of analyzing power in the system.

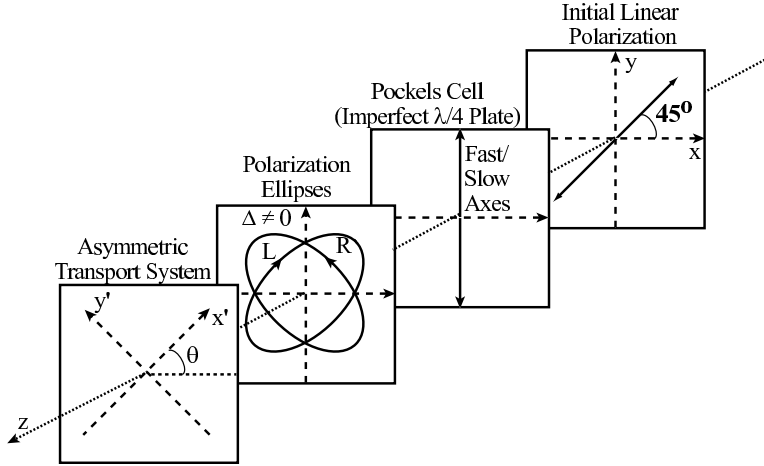


FIG. 14: Incident linear polarization is nearly circularly polarized by the Pockels cell. The error phase Δ causes the polarization ellipses for the two helicities to have their major and minor axes rotated by 90° from each other, causing helicity-correlated transmission through an optical element with an analyzing power.

By controlling the phase Δ we can control the size of the intensity asymmetry. In particular, Δ can be chosen such that the intensity asymmetry is zero. Δ can be adjusted by changing the voltage applied to the Pockels cell according to $V_\Delta = \Delta \cdot V_{\lambda/2}/\pi$, where V_Δ is the change in Pockels cell voltage required to induce a phase shift Δ and $V_{\lambda/2}$ is the voltage required for the Pockels cell to provide a half wave of retardation (~ 5.5 kV).

The magnitude of the PITA slope is a key parameter in the source configuration. For the 1998 run, the PITA slope was set by selecting the angle of incidence of the glass slide. A value of ~ 3 ppm/V was used for production running. This value was large enough to make the slide the dominant analyzing power in the system, while remaining small enough to suppress higher-order effects that can arise from residual linear polarization. For the 1999 run, the strained cathode's QE anisotropy provided a PITA slope of as large as ~ 30 ppm/V; the value of the PITA slope could be set by choosing the orientation of the rotatable half-wave plate downstream of the Pockels cell as discussed below. This much larger analyzing power made the glass slide unnecessary, but also enhanced higher-order helicity-correlated differences in beam properties, such as position differences.

In the remainder of section, we discuss the suppression of helicity-correlated beam asymmetries. The primary techniques, described in more detail below, were to

1. Suppress the intensity asymmetry via an active feedback, the “PITA feedback.”
2. For the 1999 run, suppress position differences at the source by rotating an additional half-wave plate located downstream of the helicity-flipping Pockels cell (Fig. 2) to an orientation at which position differences appeared to be intrinsically small.
3. Gain additional suppression of position differences by properly tuning the accelerator to take advantage of “adiabatic damping” (section IV A 4).
4. For the 1999 run, suppress the intensity asymmetry of the Hall C beam by use of a second intensity-asymmetry feedback system.
5. Gain some additional cancellation of beam asymmetries by using the insertable half-wave plate (located just upstream of the Pockels cell in Fig. 2) as a means of slow helicity reversal.

2. PITA Feedback

The linear relationship between the intensity asymmetry and the phase Δ allowed us to establish a feedback loop. The intensity asymmetry was measured by a BCM located near the target and the phase Δ was corrected to zero the asymmetry by adjusting the high voltage applied to the Pockels cell by small amounts. This feedback loop was called the “PITA Feedback.” The algorithm worked as follows. The initial Pockels cell voltages for right- and left-helicity (V_R^0 and V_L^0 , respectively, with $V_R^0 \approx -V_L^0$) were determined while aligning the Pockels cell. We measured the PITA slope M approximately every 24 hours, a time scale on which it was reasonably stable. During physics running, the DAQ monitored the intensity asymmetry in real time and, every 2500 window pairs (approximately every three minutes), adjusted the Pockels cell voltages to null the intensity asymmetry measured on the preceding 2500 pairs. We referred to each set of 2500 pairs as a “minirun.” The feedback is initialized with the offset voltage set to zero and the voltages for right and left helicity set to their default values:

$$\begin{aligned}
 V_{\Delta}^1 &= 0, \\
 V_R^1 &= V_R^0, \\
 V_L^1 &= V_L^0.
 \end{aligned}
 \tag{26}$$

Using the measured value of M , we apply a correction for the n^{th} minirun according to the following algorithm. For minirun n , the Pockels cell voltages were

$$\begin{aligned} V_{\Delta}^n &= V_{\Delta}^{n-1} - (A_I^{n-1}/M), \\ V_R^n &= V_R^0 + V_{\Delta}^n, \\ V_L^n &= V_L^0 + V_{\Delta}^n. \end{aligned} \tag{27}$$

The HAPPEX DAQ was responsible for calculating the intensity asymmetry and the required correction to the Pockels cell voltages for each minirun. The correction voltage V_{Δ}^n was transmitted back to the Injector over a fiber-optic line as indicated in Fig. 2. This algorithm worked effectively; the intensity asymmetry averaged over the entire 1999 run was below one ppm, an order of magnitude smaller than the physics asymmetry.

The virtue of the PITA feedback lies in the fact that the dominant cause of intensity asymmetry is the residual linear polarization in the laser beam. By adjusting the phase Δ to suppress the intensity asymmetry, we are either minimizing the residual linear polarization or at least arranging the Stokes-1 and Stokes-2 components such that their effects cancel out.

3. The Rotatable Half-Wave Plate

The rotatable half-wave plate gives us control over the orientation of the laser beam's polarization ellipse with respect to the cathode's strain axes. To describe its utility, we extend Eq. 25 to include effects due to the half-wave plate and the vacuum window at the entrance to the polarized gun. We assume that the half-wave plate is imperfect and induces a retardation of $\pi + \gamma$, where $\gamma \ll 1$. In addition, we assume that the vacuum window possesses a small amount of stress-induced birefringence $\beta \ll 1$. The result, to first order, is

$$\begin{aligned} A_I = -\frac{\epsilon}{T} [&(\Delta - \Delta^0) \cos(2\theta - 4\psi) - \\ &\gamma \sin(2\theta - 2\psi) - \beta \sin(2\theta - 2\rho)] \end{aligned} \tag{28}$$

where ψ and ρ are orientation angles for the half-wave plate and the vacuum window fast axes, respectively, as measured from the horizontal axis. In Eq. 25, the contributions

from the half-wave plate and the vacuum window were included in the term Δ^0 . This new expression has three terms:

1. The first term, proportional to Δ , is now modulated by the orientation of the half-wave plate with a 90° period.
2. The second term, proportional to γ , arises from using an imperfect half-wave plate and also depends on the half-wave plate's orientation but with a 180° period.
3. The third term, proportional to β , arises from the vacuum window and is independent of the half-wave plate's orientation because the vacuum window is downstream of the half-wave plate. This term generates a constant offset to the intensity asymmetry.

Figure 15 shows a measurement of intensity asymmetry as a function of half-wave plate orientation angle from the 1999 run. The function fit to the data allowed us to extract the relative contributions of the half-wave plate error, the vacuum window, and the Pockels cell. The three terms contributed at roughly the same magnitude, though the offset was large enough that the curve did not pass through zero intensity asymmetry. In addition, we found, as discussed more below, that the PITA slope was usually maximized at the extrema of this curve. These facts motivated us to choose to operate at an extremum (in this case, at 1425°) in order to minimize the voltage offset required to null the intensity asymmetry.

Figure 16 shows the results of a study conducted prior to the start of the 1999 run in which the position differences were also measured using BPMs located at the 5 MeV point in the injector. We observed a fairly strong correlation between the intensity asymmetry and the position differences. It was not clear what the underlying cause of this correlation was, but it was certainly clear that by minimizing the intensity asymmetry we simultaneously suppressed position differences. For this reason, during the 1999 run our strategy was to measure the intensity asymmetry as a function of half-wave plate orientation using a Hall A BCM and to choose an orientation angle which minimized the intensity asymmetry; this orientation angle would also minimize the position differences. It would have been preferable to measure the position difference in the Injector and choose a half-wave plate orientation that minimized them directly, but such a study would have required interrupting beam delivery to Hall C for several hours, and that level of interference with an experiment running in another Hall was unacceptable. Using this strategy, we achieved position differences below

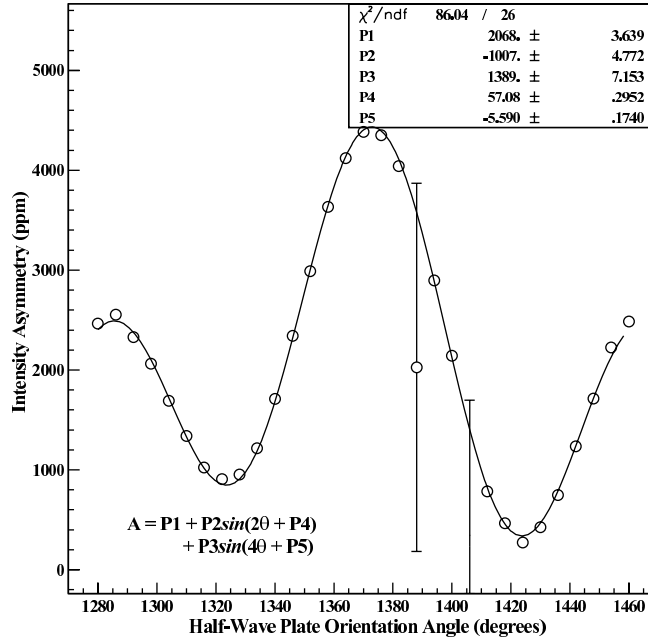


FIG. 15: Intensity asymmetry as a function of rotatable half-wave plate orientation. The error bars on some points are smaller than the symbols.

500 - 1000 nm at the 5-MeV BPMs. The position differences were further suppressed in the accelerator via adiabatic damping (section IV A 4) and some additional cancellation was achieved via the insertable half-wave plate used for slow helicity reversal.

4. Adiabatic Damping

If the sections of the accelerator are well matched and free of XY coupling, the helicity-correlated position differences become damped as $\sqrt{(A/P)}$ where A is a constant and P is the momentum. This is due to the well-known adiabatic damping of phase space area for a beam undergoing acceleration [65]. The beam emittance, defined as the invariant phase space area based on the beam density matrix, varies inversely as the beam momentum. The projected beam size and divergence, and thus the difference orbit amplitude (defined as the size of the excursion from the nominally correct orbit), are proportional to the square root of the emittance multiplied by the beta function at the point of interest. Ideally therefore the position differences become reduced by a factor of $\sqrt{(3.3 \text{ GeV}/5 \text{ MeV})} \sim 25$ between the 5 MeV region and the target. This also implies that the 5 MeV region is a sensitive location to measure and apply feedback on these position differences, if signals from the beams of

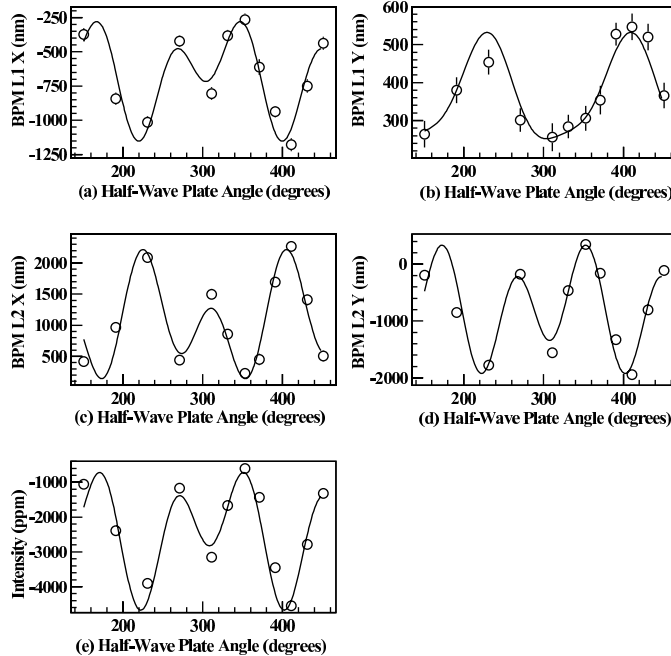


FIG. 16: Dependence of position differences measured by two BPMs at the 5 MeV point in the Injector (a-d) on the orientation of the rotatable half-wave plate. The position differences show a strong correlation with the intensity asymmetry (e). The error bars on some data points are smaller than the symbols.

the different halls could be measured separately.

Deviations from this ideal reduction factor can however occur mainly due to two effects. The presence of XY coupling can potentially lead to growth in the emittance in both X and Y planes, while a mismatched beam line often results in growth in the beta function. Both effects, as can be seen from the previous paragraph, can translate into growth in difference orbit amplitude and a reduction in adiabatic damping actually derived. The Courant-Snyder parameters [66] calculated at different sections of the accelerator based on such difference orbits are an effective measure of the quality of betatron matching, with a constant value at all sections for all orbits indicating perfect betatron matching.

Imperfections or deviations from design in the magnetic elements at the 10^{-3} level distributed across the magnet lattice, or 10^{-2} at one point in the lattice, can lead to large coupling between position and angle, or growth in one or more dimensions of phase space, and consequent amplification of the position differences. Matching the sections of the accelerator is an empirical procedure in which the Courant-Snyder parameters (or equivalently the

transfer matrices) are measured by making kicks in the beam orbit, and the quadrupoles are adjusted to fine-tune the matrix elements. This adjustment procedure is being automated [67] for future experiments.

5. *Suppressing the Hall C Intensity Asymmetry*

During the 1999 run, experiments were running in Hall C that required a high beam current (50 - 100 μA). While the PITA feedback suppressed the intensity asymmetry in Hall A, it was possible for a large intensity asymmetry to develop on the Hall C beam. Cross talk between the beams in the accelerator allowed the intensity asymmetry in the Hall C beam to induce intensity, energy, and position asymmetries in the Hall A beam.

A second feedback system on the laser power was used to control the Hall C intensity asymmetry. This feedback was based on helicity-correlated modulation of Hall C's laser intensity rather than its polarization. The modulation was introduced by adding an offset to the current driving its seed laser. We found that by manually adjusting the offset once per hour to null the Hall C intensity asymmetry, we could maintain the asymmetry at the 10 ppm level, small enough to make its effects on the Hall A beam negligible.

While adequate for a non-parity experiment, the laser-power feedback suffered from two flaws that prevented it from replacing the PITA feedback. First, the laser beam's pointing was correlated with its drive current. Thus, changing the current in a helicity-correlated way induced position differences. Second, the laser-power feedback removed the intensity asymmetry directly without correcting the underlying problem of residual linear polarization in the circularly polarized light.

B. Beam modulation

Modulation of beam parameters calibrated the response of the detectors to the beam and permitted us to measure online the helicity-correlated beam parameter differences. The beam modulation system intentionally varied beam parameters concurrently with data taking. The relevant parameters were the beam position in x and y at the target, angle in x and y at the target, and energy. We measured position differences in x and y at two points 1.3 and 7.5 m upstream of the target in a field free region, and at a point of high dispersion

in the magnetic arc leading into Hall A, as well as several other locations for redundancy. False asymmetries due to these differences were found to be negligible.

The energy of the beam is varied by applying a control voltage to a vernier input on a cavity in the accelerator's South Linac. To vary beam positions and angles, we installed seven air-core corrector coils in the Hall A beam line upstream of the dispersive arc. These coils are interspersed with quadrupoles in the beam line; their positions are chosen based on beam transport simulations intended to verify that we could span the space of two positions and two angles at the target using four of the seven coils. The additional coils are for redundancy, since a change in beam tune could change our ability to span the required space. The coils are driven by power supply cards with a control voltage input to govern their excitation. Control voltages for the seven coils and energy vernier are supplied by a VME DAC module in response to requests sent from the HAPPEX DAQ.

The coils and vernier are modulated in sequence. A modulation cycle consists of three steps up, six down, and three up, forming a stepped sawtooth pattern. Each step is 200 ms in duration. Typically the total peak-to-peak amplitude of the coil modulation is 800 mA corresponding to a beam deflection at the BPMs in the hall on the order of $\pm 100 \mu\text{m}$; for the vernier the typical amplitude is 900 keV, resulting in a deflection of similar size at the dispersion point BPM. After stepping through all seven coils and the vernier the modulation system is inactive for 38 sec, resulting in a duty factor of $\sim 33\%$.

Individual modulation cycles are evident in the BPM data (Fig. 17). It should be emphasized that these data are integrated at a subharmonic of the 60 Hz line frequency, which eliminates any 60 Hz noise in the beam position. Typically the 60 Hz noise is significantly larger than the modulations we impose. Figure 17 also shows that the response of our detectors to the beam modulation is small compared to the window-to-window noise, which is dominated by counting statistics. Only by averaging over many modulation cycles can the effects of modulation be seen in the detectors; therefore the modulation system does not add significantly to our experimental error. Section VD details how the sensitivities to beam differences are extracted from the modulation data.

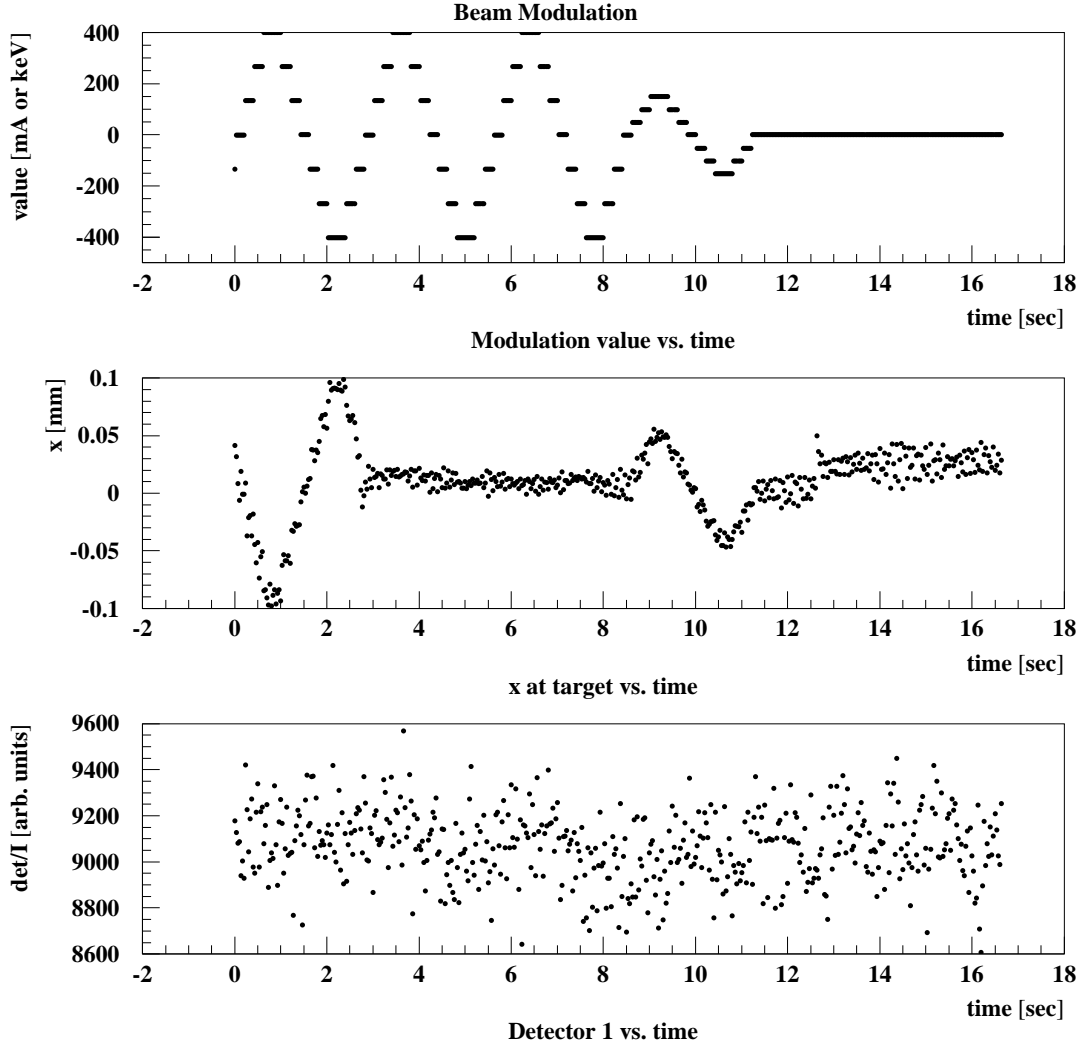


FIG. 17: Beam modulation to calibrate sensitivity. (top) Typical coil and energy vernier modulation values as a function of time. Four modulation pulses each about three seconds long are seen: the first is a horizontal correction coil, the next two are vertical coils, and the fourth is the energy vernier. (middle) Horizontal position at target versus time for the same data. The position responds to modulation of horizontal coil and energy vernier but not to modulation of vertical coils. (bottom) Čerenkov detector response versus time for the same data. Sensitivity to position and energy modulation is small compared to counting statistics.

V. ASYMMETRIES

In this section we describe how data are selected for analysis, how raw asymmetries are extracted from the data, and how these raw asymmetries are corrected for systematic effects due to helicity-correlated differences in beam parameters and to pedestals and nonlinearities in the measured signals.

A. Data selection

The 1998 production quality data were generated by 78 Coulombs of electrons striking the target; in 1999, 92 C struck the target. These totals exclude runs taken for diagnostic purposes and a small number of runs in which equipment malfunctions serious enough to compromise the quality of the entire run occurred; a typical run was about one hour.

We define a ‘data set’ as a group of consecutive runs taken with the same state (in or out) of the insertable half-wave plate; the state of the half-wave plate was changed typically after 24–48 hours of data-taking.

In our analysis of the production data, we impose a minimal set of cuts to reject unusable or compromised data. Our philosophy was never to cut on asymmetries (or helicity-correlated differences), rather only to cut on absolute quantities. We reject any data in which:

- The integrated current monitor signal falls below a value corresponding to 2% of the maximum current. In practice the threshold value was not critical since the beam was almost always either close to fully on or off.
- Any of several redundant checks for synchronization between ADC data and helicity information fails. Since the helicity state arrives in the data stream eight windows after the window it applied to, incorrect helicity assignment could result if one or more windows are missing from the data stream due to DAQ downtime. We therefore check that the second window of each pair has helicity opposite the first; that the sequence of helicity values read in hardware matches the prediction of a software implementation of the same pseudorandom bit generator; and that the scaler used to count windows increments by one at each window.

Whenever one or more consecutive windows fail one of these cuts, we also reject some windows before and after the ones that failed. For example, when the current monitor threshold cut is imposed, we also reject 10 windows before the BCM drops below threshold and 50 windows after it comes back above threshold. This procedure eliminates not only beam-off data but also conditions where the beam was ramping or the gains of our devices were recovering from a beam trip.

Additional cuts are applied depending on what is being calculated. In effect there are five different measurements being made using the same data: raw asymmetries in each of the two detectors, helicity-correlated differences in beam parameters, and sensitivities of each of the two detectors to changes in beam parameters. The additional cuts appropriate to each measurement are discussed in the following subsections.

Integrated signals for each event include: D_1 and D_2 , the Čerenkov detectors in the two arms; I_1 , I_2 , I_U , three beam current monitors (the two cavity monitors and the Unser monitor); X_1 , Y_1 , X_2 , and Y_2 , two pairs of beam position monitors (BPMs) measuring horizontal and vertical positions 7.5 and 1.3 m, respectively, upstream of the target; and X_E , a horizontal BPM located in a region of high dispersion 72.6 m upstream of the target. (These five BPMs are also denoted B_i , where $i = 1..5$.) The analysis uses detector signals normalized to the beam current, $d_{1(2)} \equiv D_{1(2)}/I_1$.

B. Calculation of raw asymmetries

For each window pair of each run we compute asymmetries for various signals S ,

$$A(S) = \frac{S^+ - S^-}{S^+ + S^-} \quad (29)$$

Superscripts + and - refer to the two states of the *Helicity* signal originating at the polarized electron source; a change in this signal corresponds to a helicity reversal of the source laser beam. The relationship of this signal to the sign of the polarization of the electron beam in the experimental hall depends on a number of factors: whether the half-wave plate is present or not in the laser table optics, the beam energy (due to precession in the accelerator arcs and the Hall A line), and the setup of the helicity Pockels cell electronics. We use the Hall A polarimeters to determine the actual polarization sign relative to the *Helicity* signal. For our 1998 and July 1999 data, with the half-wave plate in (out), the +

Helicity state corresponds to left (right) polarized electrons while the $-$ state corresponds to right (left) polarized electrons; for the April-May 1999 data the correspondence is opposite. A change in the Pockels cell configuration between May and July accounts for the latter difference, the small energy change having been compensated by adjustment of the Wien filter at the source.

For example, we compute asymmetries for each Čerenkov detector normalized by the beam current, $A_{1(2)} \equiv A(d_{1(2)})$; the summed normalized detectors, $A_s \equiv A(d_1 + d_2)$; the average value from the two detectors $A_a \equiv (A(d_1) + A(d_2))/2$; and the beam current, $A_I \equiv A(I_1)$. We also compute asymmetries for various non helicity-correlated voltage and current sources as a check for electronic crosstalk.

In addition to the cuts on beam current and data acquisition dead time, cuts are applied to reject data taken during a malfunction of the beam current monitor. For calculation of $A_{1(2)}$ and A_s we also reject data taken during a malfunction of the magnets or detector in that arm, or during times when there was significant boiling in the target.

For each run, we then compute averages of these asymmetries weighted by beam currents,

$$\langle A(S) \rangle = \frac{\sum_k w_k A(S_k)}{\sum_k w_k} \quad (30)$$

where the index k denotes pulse pair in the run and $w_k = I_{1k}^+ + I_{1k}^-$. Errors on these averages, denoted $\delta\langle A(S) \rangle$, are estimated from widths of the distributions of $A(S)$.

Finally, we compute average asymmetries over all runs in the data set

$$\langle\langle A(S) \rangle\rangle = \frac{\sum_j \epsilon_j W_j(S) \langle A(S) \rangle_j}{\sum_j W_j(S)} \quad (31)$$

where the index j denotes the run, $\epsilon_j = \pm 1$ depending on the sign of the measured beam polarization, and $W_j(S) = 1/\delta^2\langle A(S) \rangle_j$.

Figure 18 shows the asymmetries for the 1999 running periods broken down into data sets. As expected, the asymmetry changed sign when the half-wave plate was inserted, but the magnitude of the asymmetry is statistically compatible for all data sets. Similar behavior is seen for the 1998 data [6].

Our analysis assumes the asymmetry distributions are Gaussian with widths dominated by counting statistics. To check this, in Fig. 19 we plot the distribution of the quantity $((A_s)_{jk} - \langle A_s \rangle) / \sqrt{2(I_1)_{jk}}$ for the 1999 running periods. If counting statistics dominate, then the distribution of this quantity should be Gaussian. We see that this is indeed the case,

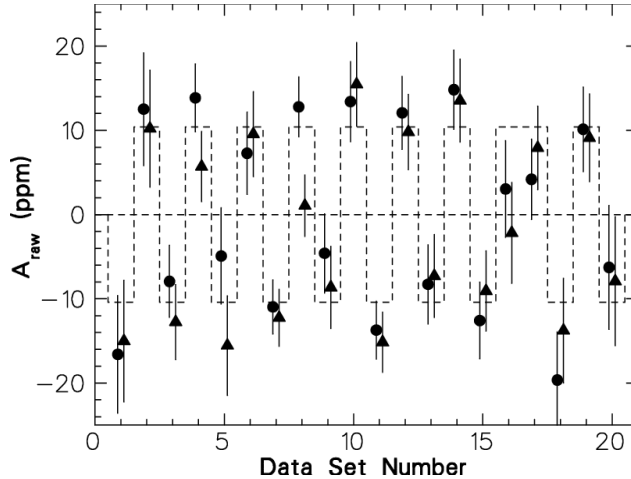


FIG. 18: Raw asymmetries for 1999 running period, in ppm, broken down by data set. The circles are for the left spectrometer, triangles for the right spectrometer. The step pattern represents the effect of insertion/removal of the half-wave plate between data sets combined with a Pockels cell reconfiguration between data sets 16 and 17; see text. The amplitude of the step is the average value of the asymmetry over the entire run.

over seven orders of magnitude with no tails. Likewise, the run averages behave statistically as can be seen in Fig. 20 where we plot the distribution of the quantity $((A_s)_j - \langle A_s \rangle) / \delta(A_s)_j$ for the 1999 running periods; the distribution is Gaussian with unit width. The 1998 data show similar behavior.

C. Calculation of helicity-correlated beam differences

For calculation of helicity-correlated beam position and energy differences, cuts are applied to reject data taken during a malfunction of the position monitors and data taken while a beam modulation device was ramping. The difference in the i th BPM is denoted $\Delta B_i = B_i^+ - B_i^-$.

Averages over each run $\langle \Delta B_i \rangle$ and over all runs in the data set $\langle \langle \Delta B_i \rangle \rangle$ are computed similarly to the asymmetry averages. For the latter, differences are weighted in the average by $W_j = 1/\delta^2 \langle A_s \rangle_j$, not by $1/\delta^2 \langle \Delta B_i \rangle_j$. The reason is that in a computation of an average corrected asymmetry $\langle \langle A_s \rangle^{\text{corr}} \rangle = \langle \langle A_s \rangle - \sum_j a_j \langle \Delta B_j \rangle \rangle$ (sec VD) the dominant error is $\delta \langle A_s \rangle$ and the average over multiple runs of $\langle \Delta B_j \rangle$ weighted by $1/\delta^2 \langle A_s \rangle$ is the relevant quantity.

Pair asymmetry residuals (normalized to current)

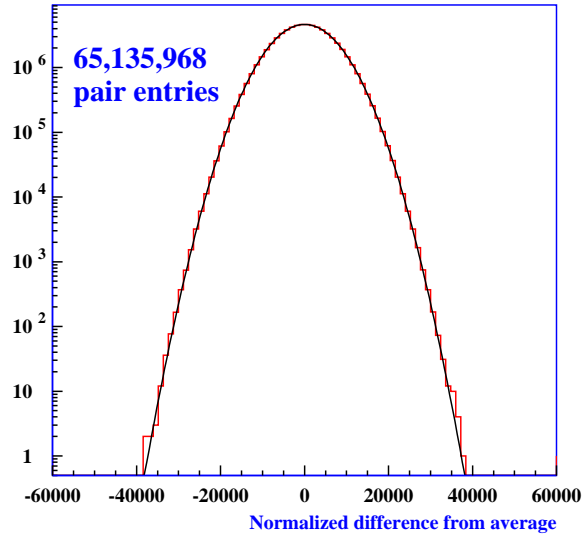


FIG. 19: Window pair asymmetries for 1999 running period, normalized by square root of beam intensity, with mean value subtracted off, in ppm.

Run asymmetry residuals (normalized to error)

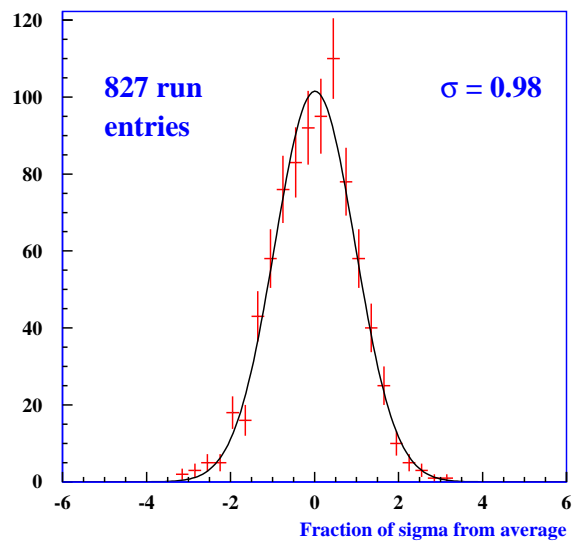


FIG. 20: Run asymmetries for 1999 running period, with mean subtracted off and normalized by statistical error.

TABLE III: Beam position differences in nm, corrected for sign of beam polarization.

	ΔX_1	ΔY_1	ΔX_2	ΔY_2	ΔX_E
1998 half-wave out	-2.7 ± 2.9	1.9 ± 1.9	-1.9 ± 3.2	1.3 ± 2.8	20.9 ± 8.5
1998 half-wave in	-2.3 ± 2.9	-1.1 ± 1.9	-2.9 ± 3.2	-0.1 ± 3.0	-0.8 ± 8.5
All 1998 data	-2.5 ± 2.0	0.4 ± 1.4	-2.4 ± 2.3	0.7 ± 2.0	10.0 ± 6.0
Apr/May 1999 half-wave out	-20.9 ± 3.1	-12.6 ± 1.5	-15.3 ± 5.2	12.7 ± 0.7	-47.3 ± 4.6
Apr/May 1999 half-wave in	-1.0 ± 3.4	-5.9 ± 1.8	-5.8 ± 5.7	-3.7 ± 0.8	18.6 ± 5.1
All Apr/May 1999 data	-11.9 ± 2.3	-9.8 ± 1.2	-11.0 ± 3.8	5.2 ± 0.5	-17.5 ± 3.4
Jul 1999 half-wave out	-9.5 ± 5.5	-44.8 ± 10.4	87.2 ± 12.4	0.3 ± 3.2	-77.0 ± 10.6
Jul 1999 half-wave in	13.9 ± 4.6	11.4 ± 8.4	-53.8 ± 11.3	-5.8 ± 2.4	60.2 ± 9.6
All Jul 1999 data	4.3 ± 3.5	-10.8 ± 6.6	10.2 ± 8.4	-3.6 ± 1.9	-1.2 ± 7.1

The BPM differences for the three running periods and two half-wave plate settings are given in Table III. Note that the differences for the two different half-wave plate states tend to have opposite sign and thus partially cancel, reducing the size of their effect on the experimental asymmetry.

D. Calculation of sensitivities to beam parameters

The helicity-correlated differences in beam parameters originate in the polarized source and can give rise to differences in rates in the detectors and therefore false contributions to the asymmetries. We compute normalized detector asymmetries corrected for beam differences using

$$\langle A \rangle^{\text{corr}} = \langle A \rangle - \langle \Delta A \rangle. \quad (32)$$

The asymmetry correction ΔA is calculated by

$$\langle \Delta A \rangle = \frac{1}{2\langle d \rangle} \left(\sum_{j=1}^5 \left(\frac{\partial d}{\partial B_j} \right) \langle \Delta B_j \rangle \right) \quad (33)$$

where $\langle d \rangle$ is the average normalized signal for the detector. We assume that the cross section is a linear function of $(x, y, \theta_x, \theta_y, E)$. Then $\partial d / \partial B_j$ is a quantity which describes the sensitivity of the detector signal to changes in a combination of beam parameters measured

by the BPM. We obtain these partial derivatives by starting with the system of linear equations

$$\frac{\partial d}{\partial C_i} = \sum_{j=1}^5 \frac{\partial d}{\partial B_j} \frac{\partial B_j}{\partial C_i} \quad (34)$$

and solving by matrix inversion

$$\frac{\partial d}{\partial B_j} = \sum_{i=1}^5 \frac{\partial d}{\partial C_i} \left(\frac{\partial B_j}{\partial C_i} \right)^{-1} \quad (35)$$

The slopes $\partial d/\partial C_i$ and $\partial B_j/\partial C_i$ describe the sensitivities of the normalized detectors and the BPMs to changes in the beam modulation devices; the index i refers to the five devices (four coils and one vernier). These slopes are calculated in offline analysis using the beam modulation data. For each modulation cycle the BPM and detector data versus coil or vernier offset value, C_i , are fit to straight lines, and the resulting slopes are averaged over each run. Values for these slopes $\partial d/\partial B_j$ averaged over each run period are given in Table IV.

We can write $\langle \Delta A \rangle = \sum_{j=1}^5 a_j \langle \Delta B_j \rangle$ where $a_j = (\partial d/\partial B_j)/2\langle d \rangle$. The coefficients a_j are stable against changes in the gains of the detectors and BCMs, as shown in Fig. 21. The helicity-correlated position differences in the beam monitors are shown in Fig. 22. Assuming negligible correlations between these coefficients and the BPM differences, we may compute corrections to asymmetries averaged over multiple runs using

TABLE IV: Summary of the detector asymmetry dependence on BPMs for the 1998 and 1999 runs. All values are given in units of ppm/ μm .

BPM	Detector 1		Detector 2	
	1998	1999	1998	1999
X_E	-0.2 ± 0.05	-0.39 ± 0.02	0.5 ± 0.05	-0.32 ± 0.02
X_1	-5.0 ± 0.7	-3.59 ± 0.09	3.5 ± 0.6	3.43 ± 0.09
X_2	10.4 ± 0.9	9.07 ± 0.03	-4.8 ± 0.8	-3.04 ± 0.03
Y_1	-0.50 ± 0.06	-0.51 ± 0.06	0.10 ± 0.05	0.61 ± 0.06
Y_2	4.7 ± 0.03	2.48 ± 0.12	0.90 ± 0.03	-1.88 ± 0.12

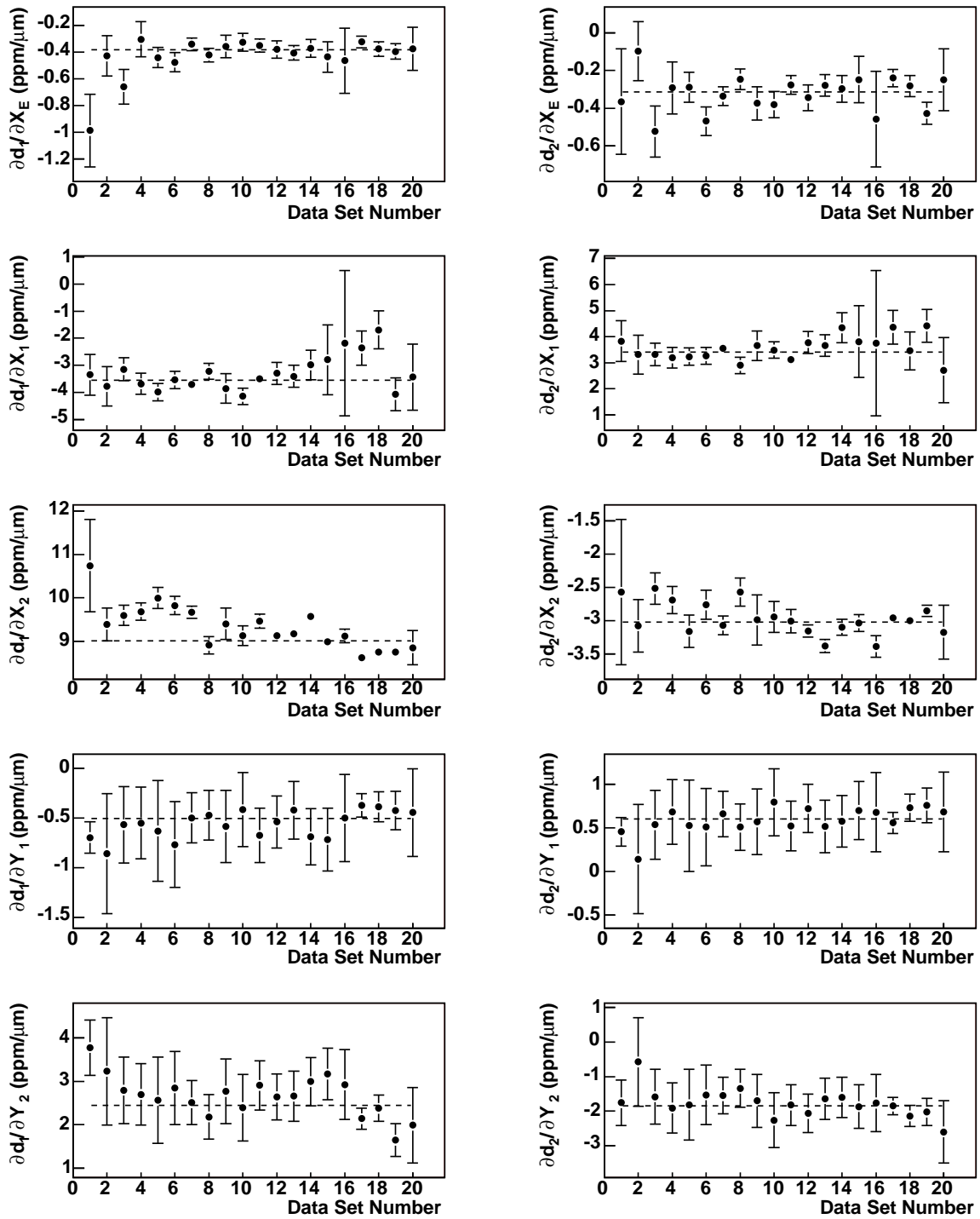


FIG. 21: Representative sensitivity coefficients $a_j = (\partial d / \partial B_j) / 2 \langle d \rangle$ vs. data set for 1999 run, for energy-sensitive position (top row), horizontal positions at locations on the beamline 7.5 m and 1.3 m upstream of the target (second and third rows), and vertical positions at 7.5 m and 1.3 m (fourth and fifth rows). Left and right columns correspond to the two detectors. Units in all cases are ppm/ μm . Coefficients are seen to be stable at the level of estimated errors.

$$\langle\langle\Delta A\rangle\rangle = \sum_{j=1}^5 \langle a_j \rangle \langle\langle\Delta B_j\rangle\rangle \quad . \quad (36)$$

The corrections for each detector as a function of the data set are shown in Fig. 23. The overall averages of the corrections are shown in Table V. The corrections are negligibly small, as are their contribution to our systematic error.

TABLE V: Asymmetry corrections in parts per billion (ppb), 1999 data.

half-wave plate state	Detector 1 (ppb)	Detector 2 (ppb)	Average correction (ppb)
out	69 ± 49	-45 ± 21	14 ± 27
in	151 ± 51	-39 ± 21	60 ± 28
combined	-36 ± 35	-3 ± 15	-20 ± 20

E. Pedestals and linearity

The signals produced by the beam monitors and Čerenkov detectors ideally are proportional to the actual rates in those devices. In reality, however, these signals can deviate from linearity over the full dynamic range and in general do not extrapolate to a zero pedestal. For illustrative purposes, suppose a measured signal, S_{meas} , is a quadratic function of the true rate, S :

$$S_{\text{meas}} = s_0 + s_1 S + s_2 S^2. \quad (37)$$

Then in the approximation where $|s_0| \ll |s_1 S|$ and $|s_2 S^2| \ll |s_1 S|$, the *measured* asymmetry is

$$A(S_{\text{meas}}) \approx A(S) \left(1 + \frac{s_2 S^2}{s_1 S} - \frac{s_0}{s_1 S} \right), \quad (38)$$

i.e. the measured asymmetry is the true asymmetry, $A(S)$, increased by the size of the quadratic piece relative to the linear piece, and decreased by the size of the pedestal relative to the linear piece (in the case where all the coefficients are positive).

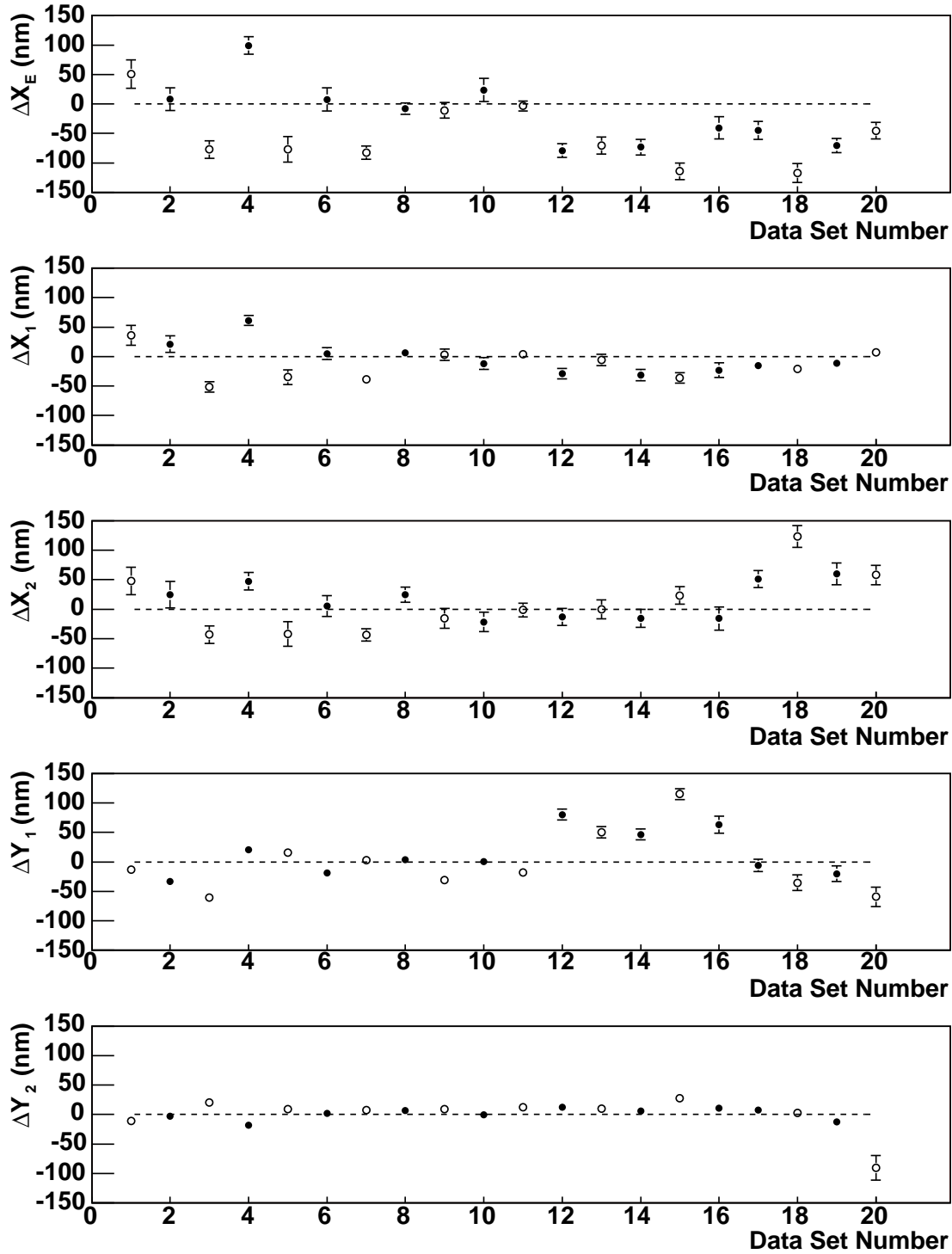


FIG. 22: Helicity-correlated position differences for 1999 run *vs.* data set, for energy-sensitive position (top plot), horizontal positions at locations on the beamline 7.5 m and 1.3 m upstream of the target (second and third plots), and vertical positions at 7.5 m and 1.3 m (fourth and fifth plots). The closed (open) circles correspond to positive (negative) polarization of the electron beam in the experimental hall. The data are plotted without correction for sign of the electron beam

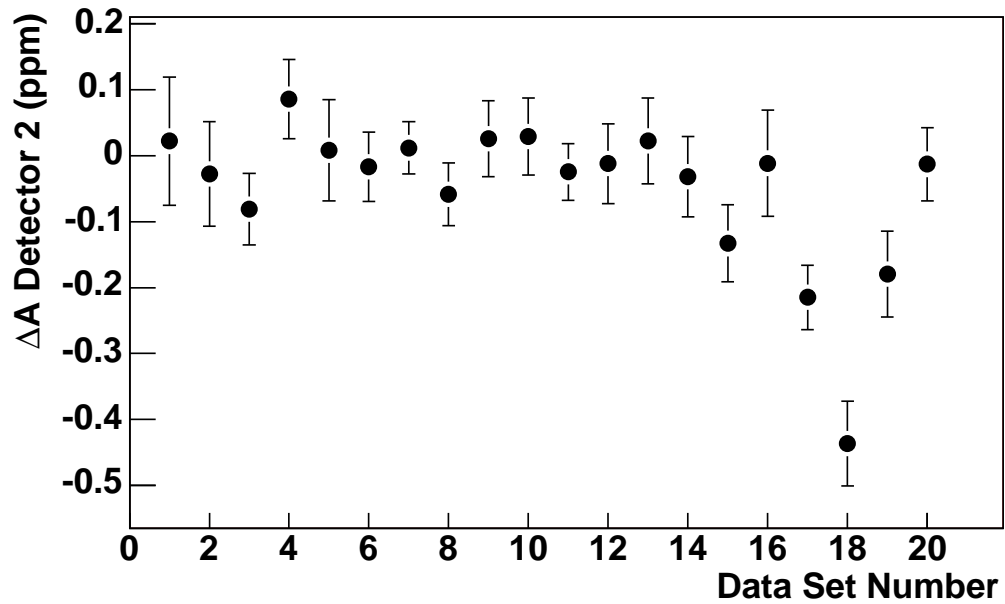
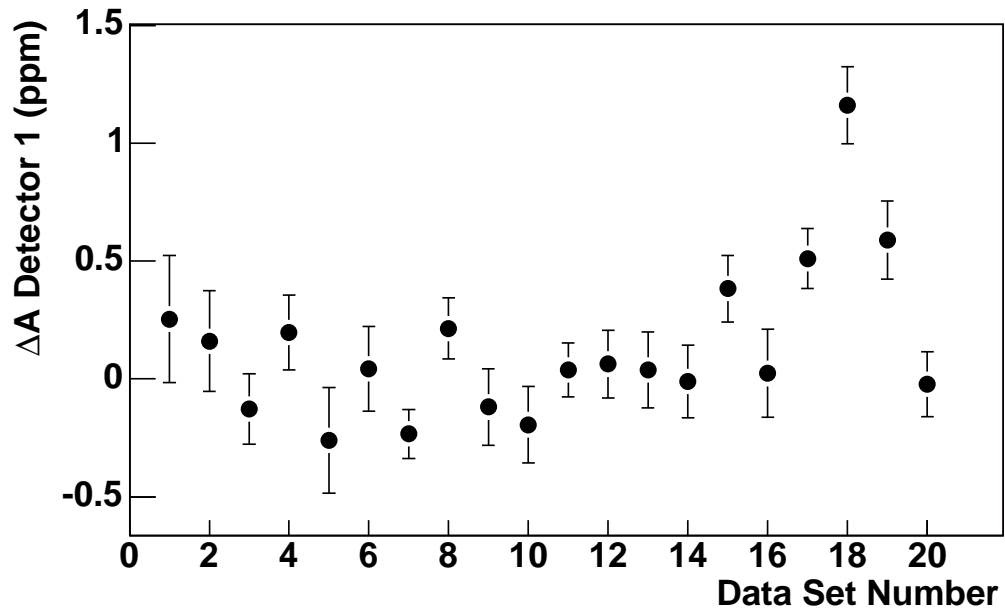


FIG. 23: Detector correction coefficients for 1999 run *vs.* data set. Note that corrections are generally consistent with zero at the level of the estimated errors. The data are plotted without correction for polarization sign.

For the normalized detector asymmetries we have $A(D_i/I) \approx A(D_i) - A(I)$. Since the average of $A(D_i)$ is an order of magnitude larger than $A(I)$, we are an order of magnitude more sensitive to detector pedestals and nonlinearities than we are to beam cavity monitor pedestals and nonlinearities.

To study the linearity of the detectors and cavity monitors, we compared them to an Unser monitor [51], a parametric current transformer which can be used as an absolute reference of current. For our purposes the Unser monitor's advantage is its excellent linearity at low currents which allows us to obtain the cavity monitor pedestals. However, the fluctuations in the Unser monitor's pedestals, which drift significantly on a time scale of several minutes, and the ordinarily small range of beam currents limited the precision of such comparisons during production data taking. Instead, we use calibration data in which the beam current is ramped up and down from zero to more than $50 \mu\text{A}$. One cycle takes about a minute. The result is that for any given beam current we have about sixty samples spread over a half hour run. This breaks any random correlation between Unser pedestal fluctuations and beam current and converts the Unser pedestal systematic to a random error.

Calibration data exist only for the 1999 run, but studies of the 1998 production data indicate nonlinearities and pedestals during that run were small in comparison to the 1998 statistics and polarimetry uncertainties.

1. *Linearity*

In order to study linearity, we make scatterplots of one signal versus another and fit each scatterplot to a straight line, using only events where $24 \mu\text{A} < I_1 < 34 \mu\text{A}$, a range in which exploratory fits suggested everything was fairly linear. We then examine the residuals between the scatterplots and the fits, relative to the signal size corresponding to about $32 \mu\text{A}$, over the full range of beam current.

Figures 24 to 25 show the results as a function of I_1 . In Fig. 24 we see the behavior of the two cavity monitors relative to the Unser monitor. Both show deviations from linearity below about $14 \mu\text{A}$ and above about $47 \mu\text{A}$, though the high-current problem for I_1 is not as clear-cut as for I_2 and the nonlinearities are at worst about 1% of the signal.

In Fig. 25 we see residuals for fits of the two detector signals versus I_1 . The nonlinear behavior at low current is due mainly to the cavity monitors. From $32 \mu\text{A}$ to over $50 \mu\text{A}$

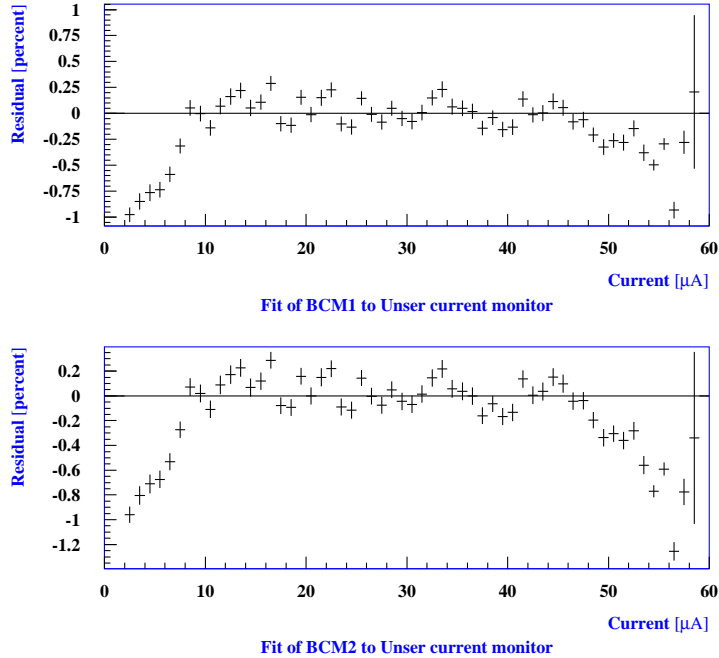


FIG. 24: (top) Residuals from fit of BCM1 to Unser data, as a fraction of the BCM1 pulse height at $32 \mu\text{A}$, versus beam current. (bottom) Same for fit of BCM2 to Unser.

the detectors are linear to well under 0.2% .

We may conclude that the detectors and cavity monitors are linear to well within the required tolerances.

2. Pedestals

Detector pedestals were measured easily, by averaging the detector signals during times when the beam is off. The resulting pedestals were always less than 0.3% of the signal corresponding to the lowest stable beam current in the production data set, and typically less than 0.06% ; these pedestals are negligible.

The cavity monitor pedestals cannot be measured this way, since the cavity signals are meaningless when the beam is off. Instead, we fit $I_{1(2)}$ to I_U in the calibration data and extrapolate to zero current. Such an extrapolation requires knowledge of the average Unser

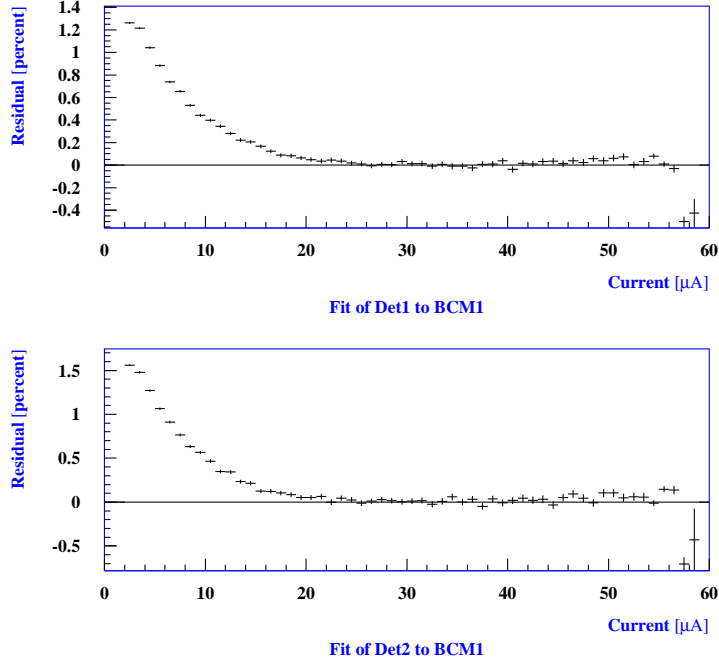


FIG. 25: (top) Residuals from fit of detector 1 to BCM1 data, as a fraction of the detector 1 pulse height at 32 μA , versus beam current. (bottom) Same for fit of detector 2 to BCM1.

pedestal, which is obtained from the beam-off data in the same run. The resulting pedestals are less than 2% of the signal corresponding to the lowest stable beam current in the production data set.

Are the cavity monitor pedestals obtained in the calibration data typical of the 1999 data? In order to answer this, we must make the reasonable assumption that the cavity monitor linearities are stable at the negligible level seen in the calibration data. If that is the case, then with negligible pedestals and nonlinearities for the detectors, a straight line fit to a scatterplot of $A(D_{\text{meas}})$ vs. $A(I_{\text{meas}})$ should give a slope equal to 1.0 if $A(I_{\text{meas}})$ is computed with a *corrected* BCM signal in which the pedestal measured in the calibration data is subtracted off. Any residual pedestals would give a deviation from unity equal to the size of the pedestal relative to the size of the signal. We find that such deviations are negligible.

3. Pedestal and linearity conclusions

No corrections for pedestals or nonlinearities need to be applied. The nonlinearities of the detectors and cavity monitors were negligible over the dynamic range of the beam current we ran. The pedestals for detectors and cavity monitors were negligible.

VI. NORMALIZATION

To extract physics results from the raw measured asymmetry, one needs to correct the beam polarization, estimate and correct for any contributions from background processes, and determine the average Q^2 of the elastically-scattered electrons, weighted by the response of the detectors. In addition one must apply radiative corrections and correct for the finite acceptance. This section describes each of these steps of the data analysis.

A. Beam polarization

Transverse components of the beam polarization are a negligible source of systematic error; the maximum analyzing power for a point nucleus is $< 10^{-8}$ [68] and the transverse component bounded by Møller polarimetry results was $\leq P_Z \sin(10^\circ)$ where P_Z is the longitudinal polarization. Explicit calculations of the vector analyzing power arising from two-photon exchange diagrams, including proton structure effects, yield an analyzing power of less than 0.1 ppm [69] for our kinematics. At different kinematics, a larger analyzing power, (-15.4 ± 5.4) ppm, was measured in the SAMPLE experiment [70], in reasonable agreement with the predicted value [69]; the much smaller value expected for our kinematics is a consequence of the higher beam energy and small scattering angle. The left-right symmetry of the apparatus further suppresses our sensitivity to transverse components. The determination of the magnitude of the polarization proceeded differently in the two running periods, and is described below.

1. 1998 Run

For the 1998 running period, we used the Mott and Møller measurements to determine the absolute beam polarization, averaged over the entire running period. This average was

used to correct the asymmetry averaged over the running period. The Compton polarimeter was not yet available. The average of 16 Mott measurements yielded a polarization of $(40.5 \pm 2.8)\%$. The quoted error is dominated by the systematic error due to extrapolation to zero target foil thickness (5% relative error), background subtraction (3%), and observed variations in the measured P_e with beam current (3%).

The average of several Møller measurements yielded $\langle P_e \rangle = (36.1 \pm 2.5)\%$, in reasonable agreement with the Mott results (note that the Møller results are 3% lower than those reported in [6], due to a subsequent recalibration of the polarization of the target foil). The uncertainty was dominated by knowledge of the foil polarization (5% relative error).

Averaging the Mott and Møller results we obtain the final result for the 1998 run of $\langle P_e \rangle = (38.2 \pm 2.7)\%$. Note that we conservatively choose not to reduce the error by $\sqrt{2}$ when averaging the results.

2. 1999 Run

For the 1999 running periods, we used the Møller measurements to determine the absolute beam polarization for each of the 20 data sets. These averages were used to correct the asymmetries averaged over each data set. Typically there were between one and three Møller measurements during each data set; these measurements were averaged to determine $\langle P_e \rangle$ for that data set. For two data sets there were no Møller measurements and $\langle P_e \rangle$ was set to the average of $\langle P_e \rangle$ for the preceding and following data sets. The polarization average over all the data sets was $(68.8 \pm 2.2)\%$.

At the time of this run, the Møller was fully commissioned, and the systematic errors were reduced by more than a factor of two. Thus we did not make regular Mott measurements, however those that were done were in reasonable agreement with the Møller results.

The Møller measurement is invasive, as it involves significantly reducing the beam current and inserting the Møller target in the beam, and so these measurements were only made at intervals. A possible concern is that the polarization may be varying between Møller measurements, and thus a non-invasive, continuous measurement of the beam polarization was desirable. This was provided in the 1999 run by the Compton polarimeter.

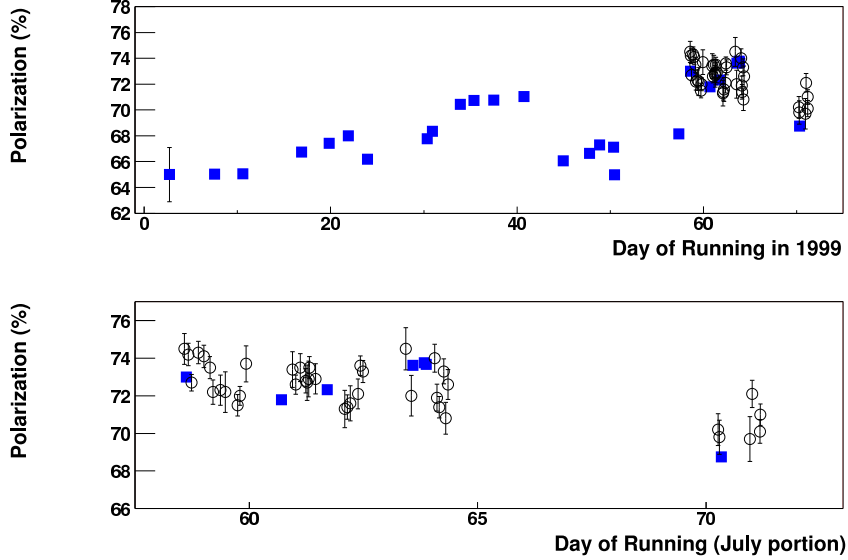


FIG. 26: Polarization of the JLab electron beam measured by the Møller (solid squares) and the Compton (open circles) polarimeters during the entire 1999 run (upper plot) and July portion (lower plot) where the Compton polarimeter was available. The error bar on the left-most Møller point in the upper plot is its total error (dominated by systematic error 3.2% relative) while all other points show only the statistical error, which for Møller data is smaller than the symbol (0.2% relative).

3. Compton Polarimeter: 1999 Run Results

Under the conditions of the 1999 run (electron beam energy of 3.3 GeV and current of $40 \mu\text{A}$) the measured Compton rate was 58 kHz and the experimental asymmetry was 1.3%. Due to the high gain of the Fabry-Perot cavity coupled to a standard 300 mW laser, a relative statistical accuracy of 1.4% was achieved within an hour, inside the analysis cuts. All the systematic errors of the measurement discussed above in section III H 3 are listed in Table II and lead to a total uncertainty of 3.3%.

Forty polarization measurements were performed by the Compton polarimeter in July 1999 in good agreement with measurements from the Møller polarimeter (see Fig. 26). They provide, for the first time, an essentially continuous monitoring of the electron beam polar-

ization with a total relative error from run-to-run of less than 2% (due to the correlations of the systematics on A_c^{th} between consecutive runs). Large variations of the beam polarization between two Møller measurements are excluded by the Compton data. More details on the Compton results are available in a separate publication [58].

Several hardware improvements have been added to the setup since then, including new front-end electronic cards and electron beam position feed-back. An electron detector made of 4 planes of 48 micro-strips is now operational and reduces the systematic errors related to the detector response.

4. Experimental asymmetries

The experimental asymmetries for the three running periods and two half-wave plate settings, corrected for the signs and magnitudes of the measured beam polarizations, are given in Table VI. For each running period, all the asymmetries are statistically compatible. The Apr/May 1999 and July 1999 results would be negligibly different if we used asymmetries and polarizations averaged over all data sets.

TABLE VI: Asymmetry results (ppm). A_1^{exp} and A_2^{exp} are the asymmetries of our two detectors normalized to beam current and corrected for sign and magnitude of beam polarization. A_s^{exp} is the asymmetry of the summed detectors, A_a^{exp} is the average of the asymmetries of the detectors, see section V B. A_I is the beam current asymmetry corrected for sign of beam polarization.

	A_1^{exp}	A_2^{exp}	A_s^{exp}	A_a^{exp}	A_I
1998 half-wave out	13.1 ± 3.7	16.0 ± 3.8	14.4 ± 2.7	14.5 ± 2.6	0.50 ± 0.21
1998 half-wave in	8.5 ± 4.0	20.8 ± 4.1	14.2 ± 2.9	14.6 ± 2.9	0.18 ± 0.26
All 1998 data	11.0 ± 2.7	18.2 ± 2.8	14.3 ± 2.0	14.5 ± 1.9	0.37 ± 0.09
Apr/May 1999 half-wave out	14.8 ± 2.2	17.1 ± 2.3	16.0 ± 1.6	15.9 ± 1.6	-0.79 ± 0.11
Apr/May 1999 half-wave in	17.1 ± 2.3	10.9 ± 2.4	13.9 ± 1.7	14.1 ± 1.7	-0.76 ± 0.14
All Apr/May 1999 data	15.9 ± 1.6	14.2 ± 1.6	15.0 ± 1.2	15.1 ± 1.1	-0.78 ± 0.09
Jul 1999 half-wave out	9.2 ± 4.5	11.7 ± 4.7	10.7 ± 3.3	10.4 ± 3.3	-0.10 ± 0.81
Jul 1999 half-wave in	20.6 ± 6.2	15.8 ± 6.6	18.1 ± 4.5	18.4 ± 4.5	0.56 ± 0.61
All Jul 1999 data	13.2 ± 3.7	13.1 ± 3.8	13.3 ± 2.7	13.2 ± 2.6	0.32 ± 0.49

Note that, for all the groups of data, A_s^{exp} (asymmetry of the summed signal from the two detectors) and A_a^{exp} (average asymmetry from the two detectors) are essentially identical, with identical widths. This indicates that the two detectors are statistically independent, demonstrating that both false asymmetries and target density fluctuations are negligibly small.

B. Backgrounds

The two backgrounds that we observed were: 1) electrons that scattered inelastically and then rebounded into the detector; and 2) electrons from the target aluminum walls. In addition, we put an upper limit on the contribution from magnetized iron in the spectrometer, based on measurements using a “proton tagging” technique, which was confirmed by simulation. In this section we describe the corrections and systematic errors due to these backgrounds.

1. *Electrons from Inelastic Scattering*

The main background to proton elastic scattering in the Hall A spectrometers near the HAPPEX kinematics comes from electrons that scattered inelastically and then re-scattered inside the spectrometer after the dipole. Much of this re-scattered debris is in the form of low energy charged or neutral particles which contribute little to the integrated signal in our calorimeter detector. The validity of this “re-scattering model” was studied with simulation of the optics, as well as with a data set of e-P elastic scattering runs with energies and angles nearby the HAPPEX running conditions. The energies varied from 3.2 to 4.0 GeV and angles from 12.5° to 35° . Several observables of background were studied from this data set, to verify that they tracked with our model. The model was applied to the HAPPEX kinematics to obtain the correction and systematic error for re-scattering from the π threshold through the Δ resonance region.

The re-scattering model is based on the assumption that the background, as a fraction of the elastic scattering signal, is given by the following integral over the energy of the scattered electron:

$$B = \int_{E_{\text{thr}}}^{E_{\text{max}}} dE P_{\text{rs}}(E) \times R(E) \quad (39)$$

where P_{rs} is the product of the probability to re-scatter in the spectrometer and the energy deposited by the scattered electron

$$P_{\text{rs}} = (\text{energy deposited}) \times (\text{re - scatter probability})$$

and $R(E)$ is the ratio of inelastic to elastic cross section,

$$R(E) = \left(\frac{d\sigma}{d\Omega dE} \right)_{\text{inel}} / \left(\frac{d\sigma}{d\Omega} \right)_{\text{elastic}}$$

and the integral extends from the inelastic threshold E_{thr} to the maximum energy loss E_{max} that could contribute, about 20% below the beam energy.

Measurements of the re-scattering function P_{rs} are shown in Fig. 27. The measurement was performed by scanning the magnetic fields in the spectrometer to force the elastically scattered electrons to follow trajectories that simulate inelastically scattered electrons; we measured the signal in the detectors as a function of the field increase. The measurements were done both with the counting technique, using the standard spectrometer DAQ, and with the integrated technique, using the integrated HAPPEX detector signal. For the individual counting technique, one measures a rate above a threshold used to trigger the DAQ, and one multiplies this rate by the amplitude in the detector; the integrating technique measures this product directly. The Δ resonance contribution is suppressed by two orders of magnitude by the spectrometers. The inelastic and elastic e-P cross sections were taken from a parameterization of SLAC data [71]. As an example, we show in Fig. 27 the ratio $R(E)$ for the HAPPEX kinematics ($Q^2 = 0.48 \text{ (GeV/c)}^2$).

In the spectrometer event-trigger data, backgrounds are identified using the following observables: 1) energy in lead glass too low; 2) momentum of electron too high; and 3) target variables outside the normal region. The target variables used were the position in the scattering plane perpendicular to the central trajectory, as well as the vertical and horizontal angles reconstructed at the collimator. The observable best correlated to the re-scattering background is the vertical angle at the target, because inelastically scattered electrons which strike near the focal plane create secondaries which have an angle that extrapolates to a position above the collimator. In Fig. 28 we show the definition of this background observable and its agreement with the model. The validity of the re-scattering model is demonstrated by the ratio of observed to predicted background, which is close to 1.0 at the HAPPEX kinematics for most observables. For some of the other observables,

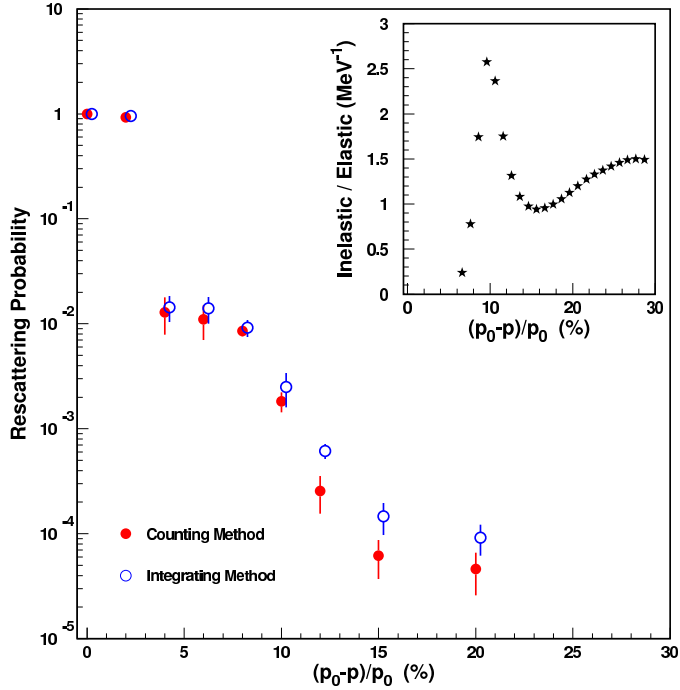


FIG. 27: Results of scan of spectrometer magnetic fields to measure the probability to re-scatter into the detector *vs.* the fractional difference from the nominal momentum setting. Inset: the ratio of inelastic to elastic cross sections at the HAPPEX kinematics, $(d\sigma/d\Omega dE)_{\text{inel}}/(d\sigma/d\Omega)_{\text{elast}}$.

the ratio was less than one since the observables measure only part of the background. Note that for this comparison, instead of using the energy-weighted re-scattering function, we use the probability to re-scatter into the focal plane which is measured by the magnet scan using the individual counting technique.

Above $Q^2 = 2$ (GeV/c)² the model under-predicts the observed backgrounds and there was a growing rate of pions seen with particle identification cuts that use the Čerenkov and lead glass detectors. However, the model works fairly well within the range $Q^2 = 0.5$ to 1.0 (GeV/c)² where there are no pions. We conclude that re-scattering in the spectrometer is the main source of background to e-P elastic scattering and is $B = (0.20 \pm 0.05)\%$ of our detected signal (Eq. 39).

The background is mainly due to the Δ resonance (see Fig. 27). To compute the correction

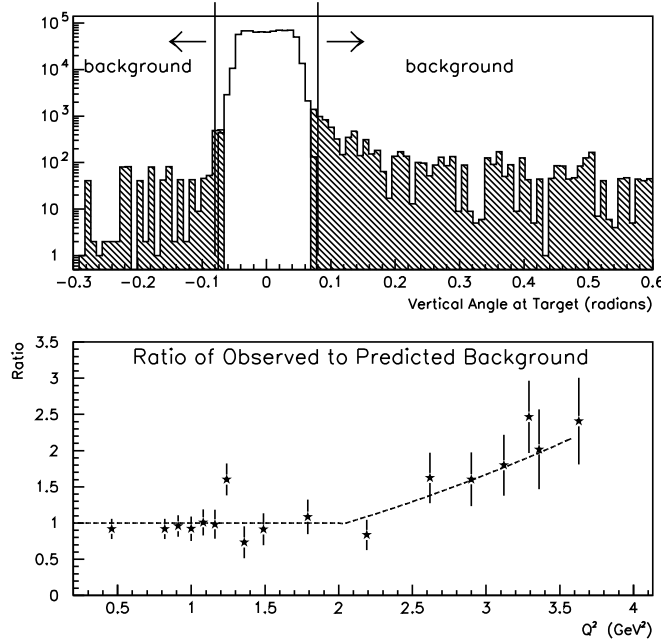


FIG. 28: Top: Reconstructed vertical angle at the target, from triggered data; background from re-scattering of inelastic electrons indicated by hatched area. Bottom: The ratio of observed to predicted re-scattering background *vs.* Q^2 ; the ratio is 1 in the region of our kinematics ($Q^2 = 0.48$ (GeV/c) 2). The line is a guide to the eye.

to our data, we use the predicted parity-violating asymmetry from the Δ resonance [72]

$$A_{\Delta}^{\text{PV}} \approx \frac{-G_F |Q^2|}{2\sqrt{2}\pi\alpha} (1 - 2\sin^2\theta_W) \quad (40)$$

The asymmetry is (-47 ± 10) ppm at our Q^2 which is 3 times as large as the asymmetry for elastic scattering. In Ref. [72], various small additional terms and theoretical uncertainties are discussed in detail, including non-resonant hadronic vector current background, axial vector coupling, and hadronic contributions to electroweak radiative corrections. The extra terms are typically 4% and have opposite signs that tend to cancel. We therefore ascribe a conservative error of 20% to the asymmetry and arrive at a correction to our experimental asymmetry of (0.06 ± 0.02) ppm, where the error includes the estimated systematic error of the re-scattering model.

2. Quasielastic Scattering from the Target Walls

Scattering from the target aluminum windows contributed $(1.4 \pm 0.1)\%$ to our detected signal. This background can be observed in the reconstructed target position in the region of momentum above the elastic peak, where one sees an enhancement in the target window regions which is due to quasielastic scattering. A more direct measure of this background was performed by inserting into the beam an empty aluminum target cell, similar to the one used to contain liquid hydrogen, and measuring the signal in our detector. The thickness of the empty target cell walls is about 10 times that of the walls used in the hydrogen cell, in order to compensate for the radiative losses in the hydrogen cell.

The correction to our data arises from the neutrons in the aluminum target. The kinematic setup of the spectrometer selects electrons which have scattered quasielastically from protons and neutrons in the aluminum. For quasielastic scattering from a nucleus with Z protons and N neutrons, the expected parity-violating asymmetry is [73]

$$A_{\text{QE}}^{\text{PV}} = \frac{-G_F|Q^2|}{4\sqrt{2}\pi\alpha} \frac{W^{\text{PV}}}{W^{\text{EM}}} \quad (41)$$

where, following the notation of [73],

$$W^{\text{EM}} = \epsilon[Z(G_E^p)^2 + N(G_E^n)^2] + \tau[Z(G_M^p)^2 + N(G_M^n)^2]$$

and

$$W^{\text{PV}} = \epsilon[ZG_E^p\tilde{G}_E^p + NG_E^n\tilde{G}_E^n] + \tau[ZG_M^p\tilde{G}_M^p + NG_M^n\tilde{G}_M^n]$$

where the G 's are nucleon electromagnetic form factors, the \tilde{G} 's are the weak nucleon form factors, ϵ, τ are the usual kinematic quantities (see definitions after Eq. 5) and we have neglected small axial vector and radiative correction terms. The predicted asymmetry for quasielastic aluminum scattering is -24 ppm at our Q^2 . We obtain a correction (0.12 ± 0.04) ppm, where we have assumed that the asymmetry from this process is known with a relative accuracy of 30%.

3. Magnetized Iron in the Spectrometer

Scattering from the magnetized iron in the spectrometer is a potential source of systematic error because of the polarization dependent asymmetry in \vec{e}, \vec{e} scattering (Møller scattering). In this section we describe the analysis which led to an upper bound for this effect.

Using the two HRS spectrometers we performed “proton tagging” measurements in which we used protons from elastic e-P scattering to tag the trajectories of electrons. We set up the two spectrometers slightly mispointed, so that for electrons that come close to the edge of the acceptance, the corresponding protons are well within the proton arm acceptance. Thus, the protons can tag electrons which might hit the magnetized iron of the pole tips.

To measure the backgrounds in the electron spectrometer we use the lead glass detector, which is read out in a bias-free way for every proton trigger or other triggers. In the low-energy tail of the energy spectrum, which contains backgrounds, we measure the excess energy for events in which the electrons come closest to the pole tips. The excess is measured relative to the energy spectra for electrons in the middle of the acceptance. No enhancement was seen for the “poletip scattering” candidate events, and we placed an upper bound that $\ll 10^{-4}$ of the energy in our detector arises from poletip scattering.

Simulations of the magnetic optics confirmed these observations. The acceptance of the spectrometer is defined primarily by the collimators, and secondarily by the first two quadrupoles in the QQDQ design. Practically no high-energy rays strike magnetized iron. In addition, secondaries from reactions in which particles which have struck the first elements of the spectrometer tend to be low energy and get swept away before hitting the detector.

The correction to our data from poletip scattering is

$$dA = f P_{e1} P_{e2} A \tag{42}$$

where f is the fraction of our signal ($f \ll 10^{-4}$), P_{e1}, P_{e2} are the polarizations of the scattered electron and the electron in the iron ($P_{e1} \sim 0.8$ and $P_{e2} \sim 0.03$), and A is the analyzing power $A \leq 0.11$. The result is conservatively $dA \ll 0.26$ ppm and we make no correction for this effect.

4. Backgrounds in HAPPEX Triggered Data

Backgrounds could be studied under the conditions of the experiment by using the HAPPEX detector to define the trigger. A signal above a discriminator threshold was used to trigger the spectrometer DAQ and read out the drift chambers and other detectors.

One small source of backgrounds was electron scattering from the aluminum frame of the HAPPEX detector, observed in a correlation between the amplitude in the detector

and the track position. At the location of the detector frame a small enhancement $\sim 10^{-3}$ in low energy background was seen which in addition should have the same asymmetry and is therefore a negligible systematic. The neutral particle component of background from the HRS was measured as the energy-weighted sample of events which had no track activity, and was a $\leq 0.2\%$ background. For the charged particle component, the method of analyzing the background was similar to what was described above for the e-P runs. We reconstructed tracks and traced them back through the spectrometer to the collimator. The percentage of tracks that miss an aperture is a measure of the background as well as other problems including mis-reconstruction. One complication of placing the HAPPEX detector near the drift chambers was that secondaries from showers splashed back into the chambers, causing confusion in the reconstruction. In event displays such events were often ambiguous with other background candidate events and could not be easily subtracted by a pattern recognition algorithm. Other chamber problems included inefficiency, scattering inside a chamber, two-track confusion due to overlap of two events, and events in which an abnormal array of hits with bad fit χ^2 existed in only one of the four chambers. This latter category was easily eliminated. We eliminated many of the two-track events by rejecting events in which one of the tracks had a good fit and was within 0.2 GeV of the elastic peak. From the remaining sample, we obtained an upper bound $\leq 0.5\%$ background which is a weaker upper bound than that obtained from the re-scattering model. Because of the limitations in reconstructing events at the 10^{-3} level we consider the re-scattering model to be a more accurate assessment of our background.

5. *Summary on Backgrounds*

Table VII lists the backgrounds, the correction to our data, and the systematic error. The total correction was $+(0.18 \pm 0.04)$ ppm, which represents a $(1.2 \pm 0.3)\%$ correction to the experimental asymmetry.

C. **Measurement of Q^2**

The square of the four-momentum transfer is $Q^2 = 2EE'(1 - \cos(\theta))$ where the three ingredients needed are the incident energy E , final energy of the electron E' , and the scattering

TABLE VII: **Backgrounds and Corrections.**

Source	Fraction Events	A (ppm)	Correction (ppm)
Inelastic e^-	0.2 %	-47	0.06 ± 0.02
Al walls	$(1.4 \pm 0.1)\%$	-24	0.12 ± 0.04
Magn. Iron	$\ll 10^{-4}$	≤ 2700	none

angle θ . For elastic scattering one may eliminate one of the three variables, which provides a consistency check. The kinematics were $E \sim 3.3$ GeV, $\theta = 12.5^\circ$ (see table Table VIII).

The beam energy is measured by two methods to an accuracy of about 1 MeV. One apparatus, called the arc method [74], measures the deflection of the beam in the arc of magnets that lead into the experimental hall, for which the integral of the field is precisely known. A second apparatus, called the e-P method [75], measures the kinematics in e-P coincidences on hydrogen. When we assumed that beam energy was correctly measured in the 1999 run, we found that an -8 MeV (-0.2%) adjustment was needed for the Q^2 in the 1998 run to be consistent with elastic scattering after known corrections for angle and momentum calibration of the scattered electron. Based on this, and based on the history of comparisons of the two energy apparatus, we have assigned a very conservative 10 MeV error to our energy measurement.

A second ingredient required for the Q^2 determination is the momentum of the scattered electron. We adjusted the momentum scale by a few tenths of a percent in order to satisfy the missing mass constraint for elastic scattering. Subsequently, the magnet constants were measured by an independent group and found to agree within 0.1% of our values.

The largest error in Q^2 comes from the scattering angle. There are two ingredients here: 1) surveys measure the angle of the spectrometer's optic axis relative to the incident beam direction; and 2) the spectrometer reconstruction code reconstructs the horizontal and vertical angles at the target relative to the optic axis using tracking detectors in the focal plane. Calibration of the optical transfer matrix for the spectrometers is performed by sieve slit runs in which the optical transfer matrix of the spectrometers is calibrated in the following way. A 0.5 cm thick tungsten plate with a rectangular pattern of holes covering the acceptance (sieve slit) is placed at the entrance of the spectrometers, and tracks in the focal plane are used to reproduce the hole pattern through a χ^2 minimization procedure.

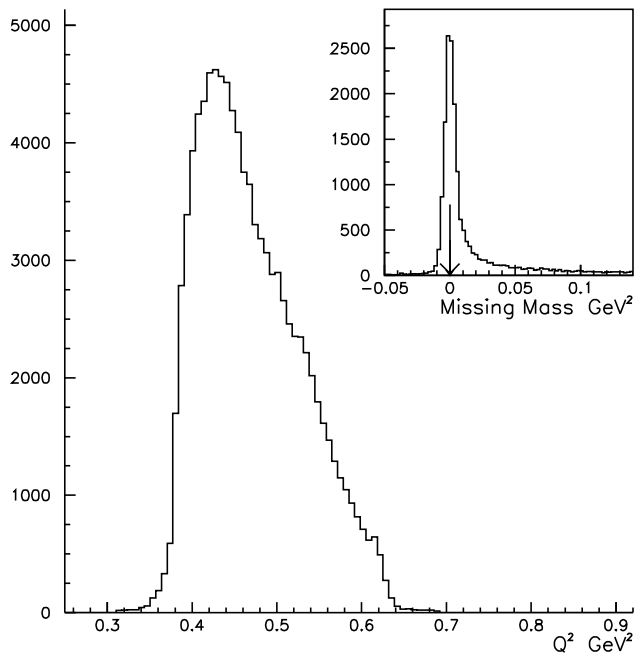


FIG. 29: Typical Q^2 spectrum measured during HAPPEX. In the inset is a missing mass spectrum from the same data.

Location of this sieve slit requires additional survey information. The combined error in these ingredients gives a 1 mrad error in the scattering angle.

The measurements of Q^2 from the 1998 and 1999 runs are given in Table VIII. These take into account the average energy loss in the target and a weighting by amplitudes in the HAPPEX detector according to $Q^2 = (\sum Q_i^2 A_i) / (\sum A_i)$ where A_i are ADC amplitudes in bin i and Q_i^2 is the corresponding measurement. This weighting shifted Q^2 by $(-0.38 \pm 0.05)\%$. A typical Q^2 distribution and missing mass spectrum is shown in Fig. 29.

In Table IX we summarize the errors which add in quadrature to 1.2% or ± 0.006 (GeV/c)² for each spectrometer. The matrix element error is an estimate of the instability in the fitting procedure for the sieve slit calibration. The estimate of time drifts was based on the observed variation with time of Q^2 and the observed time variation in the results from sieve slit runs and surveys.

The asymmetries presented in Table VI were obtained at slightly different values of Q^2 (see Table VIII). We used A_a^{exp} , the average of the asymmetries of the detectors. To combine these, the asymmetries were first corrected for background as described in the previous section, and then extrapolated to a common $Q^2 = 0.477$ (GeV/c)² using the leading Q^2

TABLE VIII: Q^2 for 1998 and 1999 HAPPEX Runs

	1998 Run	1999 Run (I)	1999 Run (II)
Beam Energy (GeV)	3.345	3.353	3.316
L-arm Angle	12.528°	12.527°	12.527°
R-arm Angle	12.558°	12.562°	12.562°
L-arm Q^2	0.473	0.477	0.466
R-arm Q^2	0.475	0.477	0.466
(GeV/c) ²			
Q^2 Error	±0.006	±0.006	±0.006

TABLE IX: Summary of Errors in Q^2

Error Source	Error	Error in Q^2
Timing Calibration	≤ 5 nsec	≤ 0.1%
Beam Position	0.5 mm	0.5%
Survey of Spectr. Angle	0.3 mrad	0.3%
Survey of Mispointing	0.5 mm	0.5%
Survey of Collimator	0.5 mm	0.5%
Target Z position	2 mm	0.3%
Momentum Scale	3 MeV	0.1 %
Beam Energy	10 MeV	0.3 %
Matrix Elements		0.4 %
Drifts in Time		0.5 %
Total Systematic Error		1.2 %

dependence from Eq. 5. The resulting weighted average asymmetry was

$$A^{\text{exp}} = -15.05 \pm 0.98 \pm 0.56 \text{ ppm}, \quad (43)$$

where the first error is statistical and the second error is systematic. This latter includes the

errors in the beam polarization, background subtraction, helicity-correlated beam properties, and Q^2 .

D. Finite Acceptance

To interpret the experimental asymmetry given in Eq. 43, one must correct for the effect of averaging over the finite acceptance of the detectors and the effect of radiation on the effective kinematics of the measurement. A Monte Carlo simulation was developed for this purpose, and is described below.

1. Monte Carlo

As the acceptance of the HRS spectrometers is dictated by their entrance collimators, the simulation involved generating elastically scattering electrons along the length of the target, with realistic account of the materials in the target region, and tracking the events to the collimators. First-order magnetic optics of the spectrometers were then used to determine the location and momentum of the electrons at the focal plane detectors. The measured analog response of the focal plane detectors, as a function of the position of the hit along the detector, was taken as a weighting factor on the asymmetry (this weighting had a $\sim 1\%$ effect compared to pure counting statistics). Account was taken of ionization energy loss in the target, both before and after the scattering.

Bremsstrahlung was included in the simulation in both the initial and final state. In the extreme relativistic limit, hard photon radiation is strongly peaked in the forward angle, and so the angle peaking approximation [76] was adopted.

The radiated cross section σ^{rad} was calculated as a convolution of integrals along the incident and scattered electron directions [77]. With E_s the incident electron energy, E_p the final electron energy, t the location of the scattering along the target of length T , $t_1(t)$ and $t_2(t)$ the material thickness in radiation lengths before and after the scattering respectively, we have

$$\sigma^{\text{rad}}(E_s, E_p) = (1 + \delta_f) \int_0^T \frac{dT}{T} \int_0^1 dy_1 I_1(y_1, t_1) \int_0^1 dy_2 I_2(y_2, t_2) \sigma(E'_s, E_p^{\text{max}}) \Theta(E_p - E_{\text{cut}}) \quad (44)$$

where y_1 and y_2 are the fractional radiative energy losses before and after the scattering, $\sigma(E'_s, E_p^{\max})$ is the unradiated cross section for elastic scattering of electrons of energy $E'_s = E_S(1 - y_1)$ into energy E_p^{\max} , where

$$E_p^{\max} = \frac{E'_s}{1 + 2(E'_s/M) \sin^2(\theta/2)} \quad (45)$$

with M the proton mass and θ the scattering angle; the final electron energy is therefore $E_p = E_p^{\max}(1 - y_2)$. The lower-energy cutoff in the spectrometer acceptance is E_{cut} . The intensity factors $I_1(y_1, t_1)$ and $I_2(y_2, t_2)$ are given by

$$I(y, t) = \frac{\Phi(y, t)}{y} \exp\left(\int_1^y dy' \frac{\Phi(y', t)}{y'}\right) \quad (46)$$

with

$$\Phi(y, t) = t_v(1 - y) + \frac{4}{3}t \left(1 - y + \frac{3}{4}y^2\right) \quad (47)$$

The first term represents the effect of internal bremsstrahlung, which was dealt with using an equivalent virtual radiator [77] of thickness

$$t_v = \frac{\alpha}{\pi} \left[\ln\left(\frac{Q^2}{m^2}\right) - 1 \right] \quad (48)$$

The second term in Eq. 47 represents the ‘complete screening approximation’ [78] calculation of external bremsstrahlung.

Finally, the factor $(1 + \delta_f)$ in Eq. 44 is the lowest order correction to the running coupling constant $\alpha^2(Q^2)$,

$$\delta_f(Q^2) \approx \frac{2\alpha}{\pi} \left[\frac{13}{12} \ln\left(\frac{Q^2}{m^2}\right) - \frac{28}{18} \right] \quad (49)$$

The primary effect of bremsstrahlung was to radiate about 20% of the elastic events out of the detector acceptance, and to lower the effective Q^2 by about 0.1%, a negligible amount.

2. Effective Kinematics

Due to both the finite acceptance of the spectrometer and radiative energy losses, the measured asymmetry represents a convolution over a range of Q^2 . To account for this, and to present a value of the asymmetry for a single Q^2 , we calculated an average incident electron energy and effective scattering angle for the experiment, and then used the simulation to calculate the factor needed to correct the acceptance-averaged asymmetry to that from point scattering at the effective kinematics.

The effective kinematics were calculated from the most probable value of the incident beam energy E_s , including energy loss in the target, as

$$E_s = \left\langle E_{\text{beam}} - \frac{dE}{dx}t \right\rangle . \quad (50)$$

Using the measured average Q^2 , the effective scattering angle θ_{eff} was found from

$$\cos(\theta_{\text{eff}}) = \frac{1 - (Q^2/(2E_s^2))(1 + E_s/M)}{1 - (Q^2/(2E_s^2))(E_s/M)} . \quad (51)$$

To obtain the correction factor, the simulation was run using a theoretical point asymmetry $A(E_s, \theta_{\text{eff}})$ at the effective kinematics. The ratio of this to the averaged asymmetry A_{MC} extracted from the simulated data was then used to extract the correction factor

$$C_{\text{finite}} = \frac{A(E_s, \theta_{\text{eff}})}{A_{\text{MC}}} = 0.993 \pm 0.010 \quad (52)$$

This correction factor was then applied to the measured asymmetry A^{exp} (Eq. 43) to yield a physics asymmetry A^{phys} at the effective kinematics:

$$A^{\text{phys}} = C_{\text{finite}} A^{\text{exp}} = -14.92 \pm 0.98 \text{ (stat)} \pm 0.56 \text{ (syst)} \quad (53)$$

for the average kinematics $Q^2 = 0.477 \text{ (GeV/c)}^2$ and $\theta = 12.3^\circ$.

In the calculation of C_{finite} , the default values for the electromagnetic form factors discussed below in Section VII A were used. The strange quark form factors were assumed to be zero for the baseline value of C_{finite} . Various available models for the Q^2 evolution of non-zero strange form factors were also simulated, and the most extreme case was used to estimate a model-dependent error on C_{finite} of 0.9%. As mentioned, C_{finite} includes the effect of bremsstrahlung, and the weighting by the detector's analog response. Uncertainties due to these effects, including errors in the beam energy and direction contributed 0.15% to the error in C_{finite} . Note that overall correction due to finite acceptance *etc.* to the measured asymmetry is much smaller than the statistical error on our measurement.

Table X summarizes all corrections and systematic errors applied to the measured asymmetries in Table VI to obtain the physics asymmetry of Eq. 53.

TABLE X: Asymmetry corrections and systematic errors.

Source	Correction	$\delta A/A(\%)$	
		(1998)	(1999)
Statistics	–	13.3	7.2
P_e	–	7.0	3.2
Q^2	–	1.8	1.8
Backgrounds	1.2	0.6	0.6
Radiative corrections	-0.1	0.1	0.1
Finite acceptance	0.7	0.9	0.9

VII. RESULTS AND INTERPRETATION

A. Electromagnetic and Axial Form Factors

The extraction of the strange quark form factors G_E^s and G_M^s from the measured asymmetry (Eq. 53) requires knowledge of the other form factors entering into Eq. 5: the purely electromagnetic form factors $G_E^{\gamma p}$, $G_M^{\gamma p}$, $G_E^{\gamma n}$, and $G_M^{\gamma n}$, as well as the neutral weak axial form factor G_A^{Zp} . Uncertainties in these form factors contribute significantly to the total uncertainty in the extracted strange form factors.

In the time since our initial publications [6, 7], there has been considerable progress made on precision measurements of these form factors (see [79] for a review). In the following we describe how values for the form factors, interpolated to our Q^2 , were extracted from world data, and we reassess our extraction of the strange form factors in light of the recent data.

1. G_A^{Zp}

As mentioned earlier, the contribution of the neutral weak axial form factor G_A^{Zp} to the measured asymmetry is suppressed for our kinematics (forward-angle scattering, where ϵ' is small). This form factor can be decomposed into terms involving the well-known charged-current axial form factor and Δs , the first moment of the strange quark momentum distributions. The latter, as measured in deep inelastic scattering, while not precisely measured, is small for our purposes [16]. The former at $Q^2 = 0$ is the axial vector coupling constant

g_A , which is well measured [47], and the Q^2 evolution of the form factor is well reproduced with a dipole form. However, G_A^{Zp} suffers from large electroweak radiative corrections, which include hadronic uncertainties, and which are problematic to calculate. These corrections have been calculated by Zhu *et al.* [87], and lead to a predicted effect on our measured asymmetry of 0.56 ± 0.23 ppm (the hadronic uncertainties in the axial radiative correction dominate the error on this prediction).

This prediction was cast into some doubt with the results from the SAMPLE collaboration on backward-angle parity-violating quasielastic scattering from a deuterium target [81]. When combined with their measurement on a hydrogen target [82, 83], they extracted a value for G_A^{Zp} in significant disagreement with the calculation of Zhu *et al.*, leading to speculation of large ‘anapole moment’ contributions. However, more recent data from SAMPLE, along with a reanalysis of the earlier data [84] now yields excellent agreement with the Zhu *et al.* calculation, and so there is no longer reason to doubt that the axial contribution is under adequate control.

2. $G_M^{\gamma p}$

The proton’s magnetic form factor is quite precisely known at our kinematics, and it deviates only slightly from the dipole form factor $G_D = [1 + Q^2/(0.71 \text{ (GeV/c)}^2)]^{-2}$. We adopt the value $G_M^{\gamma p}/\mu_p G_D = 0.9934$ at $Q^2 = 0.477 \text{ (GeV/c)}^2$ using the recent fit of Brash *et al.* [85]. This fit is a reanalysis of the magnetic form factor obtained from Rosenbluth separation data, using as an additional constraint the results on $G_E^{\gamma p}/G_M^{\gamma p}$ obtained with polarization transfer techniques. An almost identical value $G_M^{\gamma p}/\mu_p G_D = 0.9940$ at $Q^2 = 0.477 \text{ (GeV/c)}^2$ was found from the empirical fits of Friedrich and Walcher [86]. The value also agrees within 0.3% with the one we adopted in our earlier publication [7].

As the other electromagnetic form factors are often measured relative to $G_M^{\gamma p}$, we will express them relative to this value, and subsume its small uncertainty in the errors assigned to the other form factors.

3. $G_E^{\gamma p}$

The situation with regard to the proton's electric form factor is unsettled at present. The recent high-precision measurements from Jefferson Lab of the ratio $G_E^{\gamma p}/G_M^{\gamma p}$ using recoil polarization techniques [93, 94] differ significantly from older results that used Rosenbluth separation techniques (see [95] for a review of the situation). There are recent suggestions that this discrepancy could be the result of contributions from two-photon exchange [96, 97] which may have a large effect on the Rosenbluth separation data at large Q^2 . We note, however, that at our lower Q^2 the difference between the values of $G_E^{\gamma p}$ extracted from the recoil polarization data and those from the Rosenbluth data is small. Adopting the empirical fit of Friedrich and Walcher [86], which is based on both polarization data and Rosenbluth data at lower Q^2 , yields $G_E^{\gamma p}/(G_M^{\gamma p}/\mu_p) = 0.98$ at $Q^2 = 0.477$ (GeV/c)²; a similar value of $G_E^{\gamma p}/(G_M^{\gamma p}/\mu_p) = 0.97$ is obtained from the empirical fit of Arrington [95]. We adopt the former value with a 2% uncertainty, which is essentially the same as we used previously [7].

4. $G_E^{\gamma n}$

In our previous publications [6, 7] the largest uncertainty arising from an electromagnetic form factor was that due to the electric form factor of the neutron, $G_E^{\gamma n}$. Since those publications appeared, the situation for $G_E^{\gamma n}$ has improved dramatically, due to new precise results using polarization techniques now available from Jefferson Lab [87, 88, 89] and Mainz [90], as well as a new analysis that obtained $G_E^{\gamma n}$ from data on the quadrupole form factor in elastic electron-deuteron scattering [92]. Individual measurements now have uncertainties at roughly the 10% level, and the recent results, which conveniently bracket our Q^2 , are satisfactorily consistent.

To extract the value of $G_E^{\gamma n}$ at our Q^2 , we use the fit to a Galster form [91] provided by Madey *et al.* [88], which gives $\mu_p G_E^{\gamma n}/G_M^{\gamma p} = 0.161 \pm 0.006$ at $Q^2 = 0.477$ (GeV/c)². This fit was based on the world data from polarization measurements as well as the analysis of the deuteron quadrupole form factor. It did not include the very recently reported result of Warren *et al.* [89], however the fit agrees with the Warren *et al.* datum at $Q^2 = 0.5$ within 1σ . A similar fit was presented by Warren *et al.*, which did not include the Madey *et al.* datum, but nevertheless agreed with the Madey *et al.* result at their $Q^2 = 0.447$ (GeV/c)².

That fit also gave a value consistent within 3.6% with that from the Madey *et al.* fit at our Q^2 . To be conservative, we enlarge the error from the Madey fit to 5% and thus adopt the value $\mu_p G_E^{\gamma n} / G_M^p = 0.161 \pm 0.008$ at $Q^2 = 0.477$ (GeV/c)². The central value is essentially unchanged from that used previously [7], however the error bar has been reduced by almost a factor of 4. The contribution to the error in A^{PV} due to the uncertainty in $G_E^{\gamma n}$ is now less than those due to other form factors ($G_M^{\gamma n}$ and G_E^p); see Table XI.

5. $G_M^{\gamma n}$

The largest contribution to our error due to electromagnetic form factors is that due to the neutron's magnetic form factor, $G_M^{\gamma n}$. Results from two new experiments have appeared since our earlier publications [6, 7]. These are the measurements from Mainz of Kubon *et al.* [98] and from JLab of Xu *et al.* [99]. The former span a range of Q^2 from 0.071 to 0.894 GeV², and the later, while somewhat less precise, report data for Q^2 ranging from 0.3 to 0.6 GeV², including points ($Q^2 = 0.4, 0.5$ (GeV/c)²) close to our own kinematics.

Kubon *et al.* [98] provide an empirical fit to their data along with other recent data on $G_M^{\gamma n}$ [100, 101, 102]. While the recent results of Xu *et al.* [99] were not included in the fit, the fit does an excellent job of reproducing them, with agreement to better than 2%. We note that this agreement exhibits the compatibility of results obtained from very different experimental techniques, with different model dependences, and thus builds confidence in the values of $G_M^{\gamma n}$ extracted. Thus we adopt the Kubon *et al.* fit to interpolate to $Q^2 = 0.477$ (GeV/c)² and extract the value $(G_M^{\gamma n} / \mu_n) / (G_M^p / \mu_p) = 1.004 \pm 0.040$ (in order to be conservative, we have inflated the uncertainty in the fit from Kubon *et al.* by a factor of 3). This new value is somewhat lower than the value of 1.05 ± 0.02 adopted previously by us [7].

A different fit for $G_M^{\gamma n}$, using a somewhat different database of results, and a very different functional form, was obtained by Friedrich and Walter [86], and it yields the value $(G_M^{\gamma n} / \mu_n) / (G_M^p / \mu_p) = 1.039$ at $Q^2 = 0.477$ (GeV/c)², in reasonable agreement with the fit of Kubon *et al.*.

We note, however, that both fits discard the results of Bruins *et al.* [103] and Markowitz *et al.* [104]. The former has been criticized [105] due to potential difficulties with the extraction of their neutron detection efficiency, however a direct measurement of that efficiency is planned [106]. If the results from Bruins *et al.* are adopted at face value, this would have a

very significant effect on our extracted strange form factors. Finally, we note that there are new data from the CLAS at JLab presently under analysis, which should help clarify the situation [107].

In summary, the two significant changes that recent data have made to the information on the electromagnetic form factors, compared to that of our previous result [7], are the significantly improved precision on $G_E^{\gamma n}$ (without a change in the central value) and a change in the best estimate of $G_M^{\gamma n}$. The latter causes a shift in the extracted strange quark contribution compared to that presented in Ref. [7] (the shift is small compared to the statistical error). The effect of the form factors on the predicted asymmetry is summarized in Table XI.

TABLE XI: Electromagnetic form factors at the present Q^2 , normalized to $(G_M^{\gamma p}/\mu_p)$, and their contribution to the error in ppm on the theoretical asymmetry A^{PV} .

Form Factor	Value	δA (ppm)
$G_E^{\gamma p}/(G_M^{\gamma p}/\mu_p)$	0.98 ± 0.02	0.33
$G_E^{\gamma n}/(G_M^{\gamma p}/\mu_p)$	0.161 ± 0.008	0.15
$(G_M^{\gamma n}/\mu_n)/(G_M^{\gamma p}/\mu_p)$	1.004 ± 0.040	0.48

B. Strange Quark Form Factors

Using Eq. 5 and the result in Eq. 53, along with the calculated G_A^{Zp} and the known values of the proton and neutron form factors in Table XI, we may solve for the linear combination of strange form factors $G_E^s + \beta G_M^s$ where $\beta = \tau G_M^{\gamma p}/\epsilon G_E^{\gamma p} = 0.392$ at our kinematics. We obtain

$$G_E^s + \beta G_M^s = 0.014 \pm 0.020 \pm 0.010 \quad (54)$$

where the first error is the total experimental error (statistical and systematic errors added in quadrature) and the second error is the error due to the “ordinary” electromagnetic form factors and is dominated by $G_M^{\gamma n}$. Since [7] the central value has reduced slightly, though less than the error bar, and the error due to electromagnetic form factors has reduced. This result is consistent with zero strangeness contribution to the vector matrix elements of the proton. However, the result could also be zero due to a cancellation of G_E^s and G_M^s at our

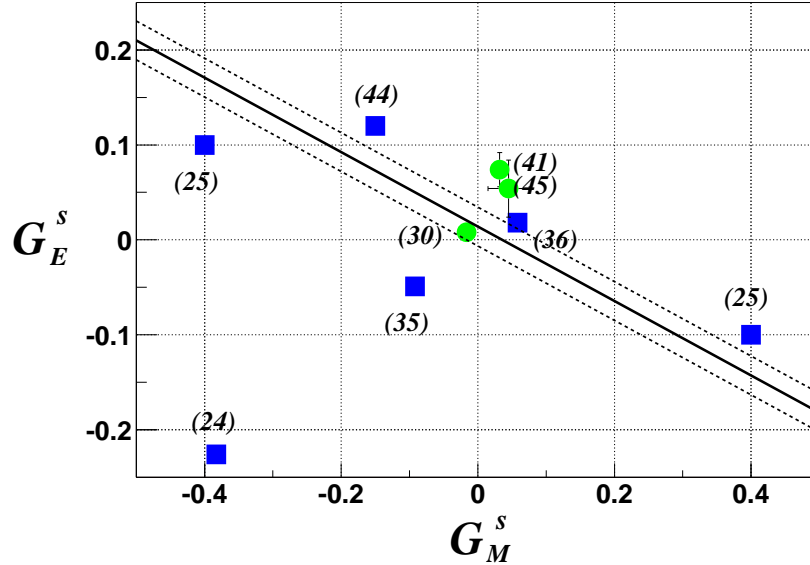


FIG. 30: Plot of G_E^s vs G_M^s at $Q^2 = 0.477(\text{GeV}/c)^2$. The band is the allowed region derived from our results. The width of the band is the total error computed in quadrature. The points are estimates from various models that make predictions at our Q^2 . The numbers in ref. [25] are plotted twice due to an ambiguity in the predicted sign. This plot is similar to Fig. 4 in [7] except that the central value and error bars have both reduced slightly, and three new models shown in circles have since been published.

Q^2 . The SAMPLE experiment [46, 83, 108], which is sensitive to G_M^s at $Q^2 = 0.1(\text{GeV}/c)^2$ as well as the axial form factor G_A^{Zp} , also found a very small strangeness contribution which is consistent with zero.

Numerous theoretical models have been formulated to predict the strangeness form factors. The problem is one of nonperturbative QCD since $m_s \simeq \Lambda_{\text{QCD}}$. In some cases the models are considered to be only an order of magnitude estimate, and in other cases only an upper bound to the strangeness effects. The large variety of models with very different physics assumptions is indicative of the difficulty in making solid predictions. See also the discussion in section II and refs [23, 24, 25, 26, 27, 28, 29, 30, 31, 32, 33, 34, 35, 36, 37, 38, 39, 40, 41, 42, 43, 44, 45].

Most models focus on predictions of the static moments ρ_s and μ_s at $Q^2 = 0$. A subset of the models attempt to predict the form factors at our Q^2 , shown as points in Fig. 30, together with our result for $G_M^s + \beta G_M^s$ displayed as a line with an error band representing the two errors in Eq. 54 added in quadrature. The numbers near the points in Fig. 30 are

the references for those models. The square points are the models displayed in Fig. 4 of our previous publication [7]. The circle points are from three models published since [7] which predict relatively small strangeness form factors that are in good agreement with our data. In two of the models [41, 45] the authors predicted a likely range (1σ) of form factors which is indicated by the error bars in the figure for those two points.

Several of the models make predictions which will be tested by future measurements, including the HAPPEX-2 experiment [109], He4 parity [110], G^0 [111], and the Mainz A4 parity experiments [112]. These measurements will be necessary to separate G_E^s and G_M^s and determine their Q^2 dependence.

VIII. CONCLUSIONS

The HAPPEX results reported in this paper have provided a stringent test of strange $q\bar{q}$ contributions to the vector matrix elements of the proton. Our results still allow for strangeness effects of a few percent or the possibility of accidental cancellation at our kinematics. It will be important to complete the program of approved parity experiments at Jefferson Lab [109, 110, 111] and elsewhere [112] to quantify the strangeness effects over a range of kinematics and over various distance scales in the nucleon. These experiments should yield a detailed mapping of the spatial dependence of $s\bar{s}$ contributions to nucleon structure.

In this paper we have reported details of the experimental technique and data analysis. We have described methods for minimizing helicity correlations of the polarized electron beam from a strained GaAs crystal. Because of the highly stable beam at Jefferson Lab we were able to acquire precise data that were nearly free of systematic error. This bodes well for future applications of parity violating electron scattering to various physics topics including future searches for strange sea effects [109, 110, 111, 112], precision studies of the standard model [113, 114] and measurements of neutron densities in nuclei [115, 116, 117].

IX. ACKNOWLEDGMENTS

We wish to thank the entire staff at Jefferson Lab for their exemplary effort in developing and operating the facility, and particularly C. K. Sinclair and M. Poelker for their

essential work on the polarized source. This work was supported by DOE contract DE-AC05-84ER40150 under which the Southeastern Universities Research Association (SURA) operates the Thomas Jefferson National Accelerator Facility, and by the Department of Energy, the National Science Foundation, the Korean Science and Engineering Foundation (Korea), the Istituto Nazionale di Fisica Nucleare (Italy), the Natural Sciences and Engineering Research Council of Canada, the Commissariat à l'Énergie Atomique (France), and the Centre National de Recherche Scientifique (France).

- [1] J. Ashman *et al.*, Phys. Lett. B **206** (1988) 364; Nucl. Phys. B **328** (1988) 527. Nucl. Phys. B **328** (1989) 1.
- [2] D. B. Kaplan and A. Manohar, Nucl. Phys. B **310** (1988) 527.
- [3] R. D. McKeown, Phys. Lett. B **219** (1989) 140.
- [4] E. J. Beise and R. D. McKeown, Comments Nucl. Part. Phys. **20** (1991) 105.
- [5] D. H. Beck, Phys. Rev. D **39** (1989) 3248.
- [6] K. Aniol *et al.*, [HAPPEX Collaboration], Phys. Rev. Lett. **82**, 1096 (1999).
- [7] K. Aniol *et al.*, [HAPPEX Collaboration], Phys. Lett. **B509**, 211 (2001).
- [8] G.A. Rutledge, Ph.D. thesis, College of William and Mary, 2001.
- [9] G.W. Miller, Ph.D. thesis, Princeton U., 2001.
- [10] J. Jardiller, Ph.D. thesis (in French), U. Blaise Pascal, 2001.
- [11] W.E. Kahl, Ph.D. thesis, Syracuse U., 2000.
- [12] T.B. Humensky, Ph.D. thesis, Princeton U., 2003.
- [13] B.T. Tonguc, Ph.D. thesis, Syracuse U., 2003.
- [14] A. O. Bazarko *et al.*, Z. Phys. C **65** (1995) 189; M. Gonchorov *et al.*, Phys. Rev. D **64** (2001) 112006.
- [15] B. Adeva *et al.*, Phys. Lett. B **302**, (1993) 533; P.L. Anthony *et al.*, Phys. Rev. Lett. **71** (1993) 959; D. Adams *et al.*, Phys. Lett. B **329** (1994) 399.
- [16] K. Abe *et al.*, Phys. Rev. Lett **74** (1995) 346.
- [17] J. Ellis and R.L. Jaffe, Phys. Rev. D **9** (1974) 1444; **10** (1974) 1669.
- [18] B. Adeva *et al.*, Phys. Rev. D **58** (1998) 112002.
- [19] K.S. Kumar and P.A. Souder, Prog. Part. Nucl. Phys. **45** (2000) S333.

- [20] D.H. Beck and R.D. McKeown, *Ann. Rev. Nucl. Part. Sci.* **51** (2001) 189.
- [21] D.H. Beck and B.R. Holstein, *Int. J. Mod. Phys. E10* (2000) 1.
- [22] M.J. Musolf *et al.*, *Phys. Rep.* **239** (1994) 1.
- [23] R.L. Jaffe, *Phys. Lett. B* **229**, 275 (1989).
- [24] H.-W. Hammer, U.-G. Meissner, and D. Drechsel, *Phys. Lett. B* **367**, 323 (1996).
- [25] H.-W. Hammer and M.J. Ramsey-Musolf, *Phys. Rev. C* **60**, 045204 (1999); *ibid* **60**, 045205 (1999); *erratum ibid* **62**, 049902 (2000); **63**, 049903 (2000).
- [26] H. Forkel, *Phys. Rev. C* **56**, 510 (1997)..
- [27] H. Forkel, M. Nielsen, X. Jin, and T. Cohen, *Phys. Rev. C* **50**, 3108 (1994).
- [28] S.-T. Hong, B.-Y. Park, and D.-P. Min, *Phys. Lett. B* **414**, 229 (1997).
- [29] P. Geiger and N. Isgur, *Phys. Rev. D* **55**, 299 (1997).
- [30] V. E. Lyubovitskij, P. Wang, Th. Gutsche, and A. Faessler, *Phys. Rev. C* **66**, 055204 (2002).
- [31] B.-Q. Ma, *Phys. Lett. B* **408**, 387 (1997).
- [32] D.O. Riska, *Nucl. Phys. A* **678**, 79 (2000).
- [33] L. Hannelius, D.O. Riska, and L.Ya. Glozman, *Nucl. Phys. A* **665**, 353 (2000).
- [34] N.W. Park, J. Schechter, and H. Weigel, *Phys. Rev. D* **43**, 869 (1991).
- [35] N.W. Park and H. Weigel, *Nucl. Phys. A* **541**, 453 (1992).
- [36] H. Weigel *et al.*, *Phys. Lett. B* **353**, 20 (1995).
- [37] U.-G. Meissner, V. Mull, J. Speth, J.W. Van Orden, *Phys. Lett. B* **408**, 381 (1997).
- [38] W. Koepf, E.M. Henley, and J.S. Pollock, *Phys. Lett. B* **288**, 11 (1992).
- [39] M.J. Musolf and M. Burkhardt, *Z. Phys. C* **61**, 433 (1994).
- [40] H. Ito, *Phys. Rev. C* **52**, R1750 (1995).
- [41] A. Silva, H.-C. Kim, and K. Goeke, *Phys. Rev. D* **65**, 014016 (2002), *Erratum-ibid. D* **66**, 039902 (2002).
- [42] T. Hemmert, U.-G. Meissner, and S. Steininger, *Phys. Lett. B* **437**, 184 (1998).
- [43] T. Hemmert, B. Kubis, and U.-G. Meissner, *Phys. Rev. C* **60**, 045501 (1999).
- [44] S.J. Dong, K.F.Liu, and A.G. Williams, *Phys. Rev. D* **58**, 074504 (1998).
- [45] R. Lewis, W. Wilcox, and R.M. Woloshyn, *Phys. Rev. D* **67**, 013003 (2003).
- [46] B. Mueller *et al.*, *Phys. Rev. Lett* **78** (1997) 3824.
- [47] Particle Data Group, R.M. Barnett *et al.*, *Phys. Rev. D* **54** (1996) 1.
- [48] M.J. Musolf and B.R. Holstein, *Phys. Rev. Lett B* **242** (1990) 461.

- [49] T. Powers, L. Doolittle, R. Ursic, and J. Wagner, Proc. 7th Workshop on Beam Instrumentation, AIP Conf.Proc. **390**, Ed. A.. Lumpkin and C.E. Eyberger (1997); JLAB-TN-96-021.
- [50] J. Alcorn *et al.*, accepted by Nucl. Instrum. Methods (2003).
- [51] K. Unser, IEEE Trans. Nucl. Sci. NS-28 (1981) 2344. T. Powers, L. Doolittle, R. Ursic, and J. Wagner, Proc. 7th Workshop on Beam Instrumentation, AIP Conf.Proc. **390**, Ed. A. Lumpkin and C.E. Eyberger (1997); JLAB-TN-96-021.
- [52] CERNOX resistor, Lakeshore Cryogenics.
- [53] Allen-Bradley, <http://www.ab.com>.
- [54] Experimental physics and industrial control system (EPICS), <http://www.aps.anl.gov/epics/>.
- [55] W.A. Watson *et al.*, CODA: A Scalable, Distributed Data Acquisition System, in Proc. of the Real Time 1993 Conference, p. 296; G. Heyes *et al.*, The CEBAF Online Data Acquisition System, in Proc. of the CHEP Conference, 1994, p. 122; D.J. Abbott *et al.*, CODA Performance in the Real World, 11th IEEE NPSS Real Time 199 Conference, JLab-TN-99-12 (1999).
- [56] C.K. Sinclair, "Electron Beam Polarimetry", Tech Note JLAB-ACC-98-04; T.J. Gay and F.B. Dunning, Rev. Sci. Instrum. **63** (1992) 1635; T.J. Gay *et al.*, Rev. Sci. Instrum. **63** (1992) 114. S. Mayer *et al.*, Rev. Sci. Instrum. **64** (1993) 952.
- [57] J.S. Price *et al.*, Proc. 13th Symposium on High Energy Spin Physics (SPIN98) Protvino, Russia, 8-12 September 1998, Ed. N.E. Tyurin, V.L. Solovianov, S.M. Troshin, and A . G. Ufimtsev, (World Scientific) 1999; JLab Technical Note ACC-97-27, 1997 (unpublished).
- [58] M. Baylac *et al.*, Phys. Lett. B **539**, 8 (2002).
- [59] D. Neyret *et al.*, Nucl. Instrum. Methods **A 443**, 231 (2000).
- [60] J.P. Jorda *et al.*, Nucl. Instrum. Methods **A 412**, 1 (1998).
- [61] N. Falletto *et al.*, Nucl. Instrum. Methods **A 459**, 412 (2001).
- [62] M. Baylac, Ph.D. thesis, U. Claude Bernard Lyon I, # 212-2000 ; Report CEA/DSM/DAPNIA/SPhN-00-05-T (unpublished).
- [63] G. D. Cates *et al.*, Nucl. Instrum. Methods, **A 278** (1989) 293-317.
- [64] T. B. Humensky *et al.*, SLAC-PUB-9381. Submitted to Nucl. Instrum. Methods **A** (2002).
- [65] D.A. Edwards and M.J. Syphers, An Introduction to the Physics of High Energy Accelerators, Wiley Interscience (1993).

- [66] E.D. Courant and H.S. Snyder, *Annals of Physics* **3**(1) (1958) 1.
- [67] Y. Chao, “Measuring and Matching Transport Optics at Jefferson Lab”, Proceedings of the 2003 Particle Accelerator Conference, Portland, Oregon, 2003.
- [68] N.F. Mott, *Proc. R. Soc. London, Ser A* **135**, 429 (1932); *ibid.* **124**, 425 (1929).
- [69] A. Afanasev, I. Akushevich, N.P. Merenkov, Workshop on Exclusive Process at High Momentum Transfer, Jefferson Lab, May 15-18, 2002; hep-ph/0208260.
- [70] S.P. Wells *et al.*, *Phys. Rev. C* **63**, 064001 (2001).
- [71] L.W. Whitlow *et al.*, *Phys. Lett. B* **282** (1992) 475; *Phys. Lett. B* **250** (1990) 193.
- [72] N.C. Mukhopadhyay *et al.*, *Nucl. Phys. A* **633**, 481 (1998).
- [73] M.J. Musolf and T.W. Donnelly, *Nucl. Phys. A* **546**, 509 (1992); Erratum-*ibid* **A 550**, 564 (1992).
- [74] D. Marchand, Ph.D. Thesis, U. Clermont-Ferrand, 1998.
- [75] O. Ravel *et al.*, *Nucl. Instrum. Methods, A* **409**, 611 (1998).
- [76] S. Stein *et al.*, *Phys. Rev. D* **12**, 1884 (1975).
- [77] L.W. Mo and Y.S. Tsai, *Rev. Mod. Phys.* **41**, 205 (1969).
- [78] Y.S. Tsai, *Rev. Mod. Phys.* **46**, 815 (1974).
- [79] H. Gao, *Int. J. Mod. Phys E* **12**, 1 (2003).
- [80] S.L. Zhu, S.J. Puglia, B.R. Holstein, and M.J. Ramsey-Musolf. *Phys. Rev. D* **62**, 033008 (2000); M.J. Musolf and B.R. Holstein, *Phys. Lett. B* **242**, 461 (1990).
- [81] R. Hasty *et al.*, *Science*, **290**, 2117 (2000).
- [82] B. Mueller *et al.*, *Phys. Rev. Lett.* **78**, 3824 (1997).
- [83] D.T. Spayde *et al.*, *Phys. Rev. Lett.* **84**, 1106 (2000).
- [84] T.M. Ito *et al.*, nucl-ex/03100001; E. Beise, private communication (2003).
- [85] E.J. Brash, A. Kozlov, Sh. Li, and G.M. Huber, *Phys. Rev. C* **65**, 051001(R) (2002).
- [86] J. Friedrich and Th. Walcher, *Eur. Phys. J A* **17**, 607 (2003).
- [87] H. Zhu *et al.*, *Phys. Rev. Lett.* **87**, 081801 (2001).
- [88] R. Madey *et al.*, *Phys. Rev. Lett.* **91**, 122002 (2003).
- [89] G. Warren *et al.*, nucl-ex/0308021
- [90] J. Bermuth *et al.*, *Phys. Lett B* **564**, 199 (2003).
- [91] S. Galster, H. Klein, K.H. Schmidt, D. Wegener, and J. Bleckwenn, *Nucl. Phys. B* **32**, 221 (1971).

- [92] R. Schiavilla and I. Sick, Phys. Lett C **64**, 041002(R) (2001).
- [93] M.K. Jones *et al.*, Phys. Rev. Lett. **84**, 1398 (2000).
- [94] O. Gayou *et al.*, Phys. Rev. Lett. **88**, 092301 (2002).
- [95] J. Arrington, Phys. Rev. C **68**, 034325 (2003).
- [96] P.A.M. Guichon and M. Vanderhaeghen Phys. Rev. Lett. **91**, 142303 (2003).
- [97] P.G. Blunden, W. Melnitchouk, J.A. Tjon, Phys. Rev. Lett. **91**, 142304 (2003).
- [98] G. Kubon *et al.*, Phys. Lett. B **524**, 26 (2002).
- [99] W. Xu *et al.*, Phys. Rev. C **67**, 012201(R) (2003).
- [100] H. Anklin *et al.*, Phys. Lett. B **336**, 313 (1994); H. Anklin *et al.* Phys. Lett B **428**, 248 (1998).
- [101] H. Gao *et al.*, Phys. Rev. C **50**, R546 (1994).
- [102] W. Xu *et al.*, Phys. Rev. Lett. **85**, 2900 (2000).
- [103] E.E.W. Bruins *et al.*, Phys. Rev. Lett. **75**, 21 (1995).
- [104] P. Markowitz *et al.*, Phys. Rev. C **48**, R5 (1993).
- [105] J. Jourdan, I. Sick, J. Zhao, Phys. Rev. Lett. **79**, 5186 (1997).
- [106] E.E.W. Bruins *et al.*, Phys. Rev. Lett. **79**, 5187 (1997).
- [107] Jefferson Lab Expt. 94-017, W. Brooks and M. Vineyard, spokespersons; W. Brooks, private communication (2003).
- [108] E.J. Beise nucl-ex/0309008; R. Hasty *et al.*, Science **290** (2000) 2117
- [109] HAPPEX-II Experiment E99-115, K.S. Kumar and D. Lhuillier, spokespersons.
- [110] He4 Parity Experiment E00-114, D. Armstrong and R. Michaels, spokespersons.
- [111] G0 Experiment E00-006, D.H. Beck, spokesperson.
- [112] Mainz A4 Parity Experiment, D. von Harrach, spokesperson.
- [113] The Q_{weak} Experiment, J. Bowman, R. Carlini, J.M. Finn, S. Kowalski, and S. Page, spokespersons.
- [114] Letter of Intent to Measure Parity Violating DIS from Deuterium, X. Zheng, spokesperson.
- [115] C. J. Horowitz, Phys. Rev. C **57**, 3430 (1998).
- [116] C. J. Horowitz, S. Pollock, P. Souder, and R. Michaels, Phys. Rev. C **63**, 025501 (2001).
- [117] The PREX Experiment, JLab proposal E03-011, P. Souder, G. Urciuoli, R. Michaels, spokespersons